Engineering proximity exchange by twisting: Reversal of ferromagnetic and emergence of antiferromagnetic Dirac bands in graphene/$Cr_2Ge_2Te_6$

Klaus Zollner* and Jaroslav Fabian
Institute for Theoretical Physics, University of Regensburg, 93040 Regensburg, Germany

We investigate the twist-angle and gate dependence of the proximity exchange coupling in twisted graphene on monolayer $Cr_2Ge_2Te_6$ from first principles. The proximitized Dirac band dispersions of graphene are fitted to a model Hamiltonian, yielding effective sublattice-resolved proximity-induced exchange parameters ($\lambda_{\rm ex}^{\rm A}$ and $\lambda_{\rm ex}^{\rm B}$) for a series of twist angles between 0° and 30°. For aligned layers (0° twist angle), the exchange coupling of graphene is the same on both sublattices, $\lambda_{\rm ex}^{\rm A} \approx \lambda_{\rm ex}^{\rm B} \approx 4$ meV, while the coupling is reversed at 30° (with $\lambda_{\rm ex}^{\rm A} \approx \lambda_{\rm ex}^{\rm B} \approx -4$ meV). Remarkably, at 19.1° the induced exchange coupling becomes antiferromagnetic: $\lambda_{\rm ex}^{\rm A} < 0, \lambda_{\rm ex}^{\rm B} > 0$. Further tuning is provided by a transverse electric field and the interlayer distance. The predicted proximity magnetization reversal and emergence of an antiferromagnetic Dirac dispersion make twisted graphene/$Cr_2Ge_2Te_6$ bilayers a versatile platform for realizing topological phases and for spintronics applications.

Keywords: spintronics, graphene, heterostructures, proximity exchange

Van der Waals (vdW) heterostructures composed of twisted monolayers [1–4] promise great tunability of electronic, optical, and magnetic properties. The most prominent example is magic-angle twisted bilayer graphene, exhibiting magnetism and superconductivity due to strong correlations [5–19]. Other platforms for correlated physics are offered by trilayer graphene [20–29] and twisted transition metal dichalcogenides (TMDCs) [30].

However, twistronics is yet to demonstrate its potential for proximity effects [31], enabling phenomena such as superconductivity [32, 33], magnetism [34–52], and strong spin-orbit coupling (SOC) [53–69] in materials — most notably graphene — lacking them. Magnetism in graphene can be induced by proximity exchange coupling with a ferro- or antiferromagnet. Of particular interest are magnetic insulators (semiconductors) such as $Cr_2Ge_2Te_6$ [39, 58, 70] (CGT) or CrI_3 [40, 49, 71, 72], which can modulate the band structure of graphene (or another nonmagnetic material) without significant charge transfer and without contributing additional transport channels. Proximity exchange effects in graphene can be observed by quantum anomalous Hall effect [73], magnetoresistance [74], or nonlocal spin transport experiments [75]. Joined with strong SOC in exso-tic heterostructures [76] proximity exchange can also induce spin-orbit torque [70, 77–79].

We already know that proximity exchange coupling in graphene can be tuned by gate [34, 80]. Can we also tune it by twisting? A recent study shows the sensitivity of the spin polarization, magnetic anisotropy, and Dzyaloshinskii-Moriya interaction to the twist angle in graphene/2H-VSeTe heterostructures [81]. Similarly, tight-binding studies predict that the strength of proximity SOC in graphene/TMDC heterostructures [82, 83] can be tuned by the twist angle. It is then natural to expect that the strength of the proximity exchange could change depending on the twist angle.

We show here that not only the magnitude, but also the orientation and even the character (ferro or antiferromagnetic) of the proximity exchange can depend on the twist angle. Employing first-principles calculations we study the twist-angle dependence of the proximity exchange coupling in large graphene/CGT supercells. From the proximitized Dirac band dispersions of graphene, which we fit to a model Hamiltonian, we extract sublattice-resolved exchange parameters, $\lambda_{\rm ex}^{\rm A}$ and $\lambda_{\rm ex}^{\rm B}$, for a series of twist angles between 0° and 30°. We find that one can tune the ferromagnetic (uniform) exchange couplings ($\lambda_{\rm ex}^{\rm A} \approx \lambda_{\rm ex}^{\rm B}$) from about 4 to -4 meV by twisting the layers. This reversal of the induced spin polarization by the twist angle is surprising when considering that the CGT magnetization orientation is unchanged.

Even more surprising is the emergence of antiferromagnetic (staggered) proximity exchange coupling at 19.1°, where $\lambda_{\rm ex}^{\rm A} < 0$ and $\lambda_{\rm ex}^{\rm B} > 0$. At this twist angle there is a delicate balance in the orbital hybridization of the spin up and spin down CGT bands with the carbon p_z orbitals, which makes the exchange coupling highly sensitive to the atomic registry. By laterally shifting the two layers, ferromagnetic couplings can be realized as well. Graphene/CGT stacks thus form a versatile platform for engineering proximity exchange coupling in graphene.

Finally, we also study the influence of strain, interlayer distance, and (transverse) electric field on the doping level, band offsets, and proximity exchange parameters, for different twist angles. We point out the crucial role of both momentum backfolding and interlayer orbital hybridization when tracing the microscopic mechanism for the observed proximity exchange tunability. One important message that our results convey is that the knowledge of the twist angle is crucial when reporting experiments on magnetic proximity effects: not only the orientation of the induced spin polarization, but also the

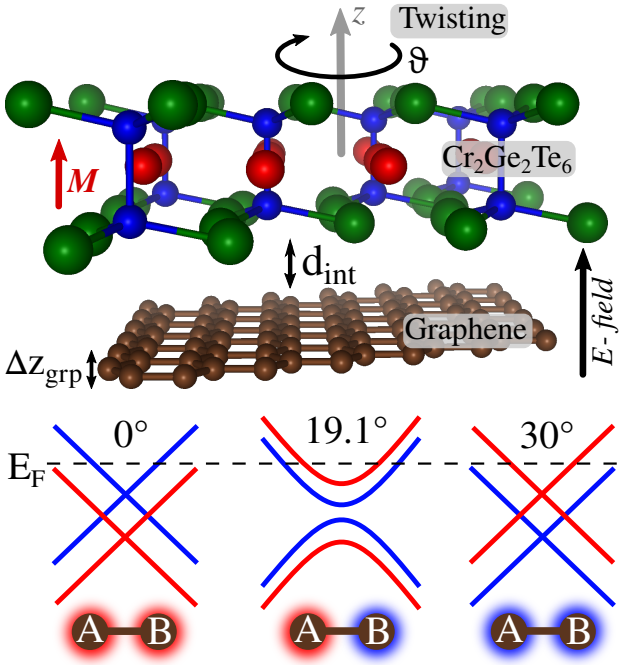

FIG. 1. 3D view of CGT on graphene, where we define the interlayer distance, d_{int}, and the rippling of the graphene layer, Δz_{grp}. We twist CGT by an angle ϑ around the z axis, with respect to graphene. The proximitized Dirac dispersions are sketched for three most relevant twist angles. Red bands are polarized spin up (defined by the CGT magnetization $\boldsymbol{M}$ along z direction), while blue bands are polarized spin down. The spin polarizations on the graphene lattice, resulting from these Dirac bands at the given Fermi level (dashed line), are also sketched.

apparent magnetic ordering (ferro- or antiferromagnetic) need not correspond to the substrate magnetic layer.

Crystal structures. We consider vdW heterostructures of graphene and CGT, with a series of twist angles, ranging from 0° to 30° in steps of roughly 3°, between the two monolayers, see Fig. 1. In order to form commensurate supercells for periodic density functional theory (DFT) calculations, we strain the monolayers in the twisted heterostructures. In Table S1 we summarize the main structural information for the twist angles we consider, see Supplemental Material (SM) [84]. After relaxation of the heterostructures, we find an average interlayer distance, $d_{\rm int} \approx 3.55$ Å, and a graphene rippling, $\Delta z_{\rm grp} < 1$ pm, nearly independent of the twist angle.

Effective low-energy Hamiltonian. From our first-principles calculations we extract the low-energy band structure of the proximitized graphene. The systems we consider have broken time-reversal symmetry with C_3 structural symmetry. The following Hamiltonian, derived from symmetry [34, 85, 86], is able to describe the graphene bands in the vicinity of the Dirac points when proximity exchange is present

$$\mathcal{H} = \mathcal{H}_0 + \mathcal{H}_\Delta + \mathcal{H}_{\rm ex} + \mathrm{E_D}, \tag{1}$$
$$\mathcal{H}_0 = \hbar v_{\rm F}(\tau k_x \sigma_x - k_y \sigma_y) \otimes s_0, \tag{2}$$
$$\mathcal{H}_\Delta = \Delta \sigma_z \otimes s_0, \tag{3}$$
$$\mathcal{H}_{\rm ex} = (-\lambda_{\rm ex}^{\rm A}\sigma_+ + \lambda_{\rm ex}^{\rm B}\sigma_-) \otimes s_z. \tag{4}$$

Here $v_{\rm F}$ is the Fermi velocity and the in-plane wave vector components k_x and k_y are measured from ±K, corresponding to the valley index $\tau = \pm 1$. The Pauli spin matrices are s_i, acting on spin space $(\uparrow, \downarrow)$, and σ_i are pseudospin matrices, acting on sublattice space ($\mathrm{C_A}$, $\mathrm{C_B}$), with $i = \{0, x, y, z\}$ and $\sigma_\pm = \frac{1}{2}(\sigma_z \pm \sigma_0)$. The staggered potential gap is Δ and the sublattice-resolved proximity-induced exchange parameters are $\lambda_{\rm ex}^{\rm A}$ and $\lambda_{\rm ex}^{\rm B}$. The four basis states are $|\Psi_{\rm A}, \uparrow\rangle$, $|\Psi_{\rm A}, \downarrow\rangle$, $|\Psi_{\rm B}, \uparrow\rangle$, and $|\Psi_{\rm B}, \downarrow\rangle$. The model Hamiltonian is centered around the Fermi level at zero energy. Charge transfer between the monolayers in the DFT calculation is captured by the Dirac point energy, $\mathrm{E_D}$, which adjusts the Dirac point with respect to the Fermi level.

Proximity induced exchange in twisted structures. In Fig. 2(a), we show the global band structure for the graphene/CGT heterostructure for a twist angle of 30°; the results for other angles and effects of interlayer charge transfer are summarized in the SM [84]. In agreement with recent calculations [39, 70], we find the Dirac cone located at the Fermi level and close to the conduction band edge of the CGT.

In Figs. 2(b)-(d) we present zooms to the Dirac bands which exhibit proximity exchange splitting. For the aligned heterostructure (0°) the exchange splitting is ferromagnetic, with equal signs on A and B sublattices. The fitted exchange parameters are $\lambda_{\rm ex}^{\rm A} \approx \lambda_{\rm ex}^{\rm B} \approx 4.2$ meV. The Dirac bands look similar for the 30° twist angle, but the spin polarizations are *reversed*, with the parameter values of $\lambda_{\rm ex}^{\rm A} \approx \lambda_{\rm ex}^{\rm B} \approx -3.6$ meV. This is rather surprising considering that the ferromagnet in both cases has the same magnetization orientation.

However, the most remarkable case is the 19.1° twist angle, shown in Fig. 2(c). The Dirac band structure does not resemble a ferromagnetic graphene at all. Instead, the spin splittings of the bands are compatible with *antiferromagnetic* exchange. Indeed, a fit to the low-energy Hamiltonian, Eq. (1), yields staggered exchange couplings, $\lambda_{\rm ex}^{\rm A} \approx -2.1$ meV and $\lambda_{\rm ex}^{\rm B} \approx 1.3$ meV. In other words, graphene proximitized by a ferromagnetic substrate can behave as an antiferromagnet.

To get the full picture of proximity exchange we plot in Fig. 3 the twist-angle dependence of ferromagnetic, $\lambda_{\rm F} = (\lambda_{\rm ex}^{\rm A} + \lambda_{\rm ex}^{\rm B})/2$, and antiferromagnetic, $\lambda_{\rm AF} = (\lambda_{\rm ex}^{\rm A} - \lambda_{\rm ex}^{\rm B})/2$, couplings (listed in Tab. S2 and Tab. S4); the magnetization of CGT is kept in the same direction for all studied angles. We find a rather continuous tunability of the ferromagnetic exchange from

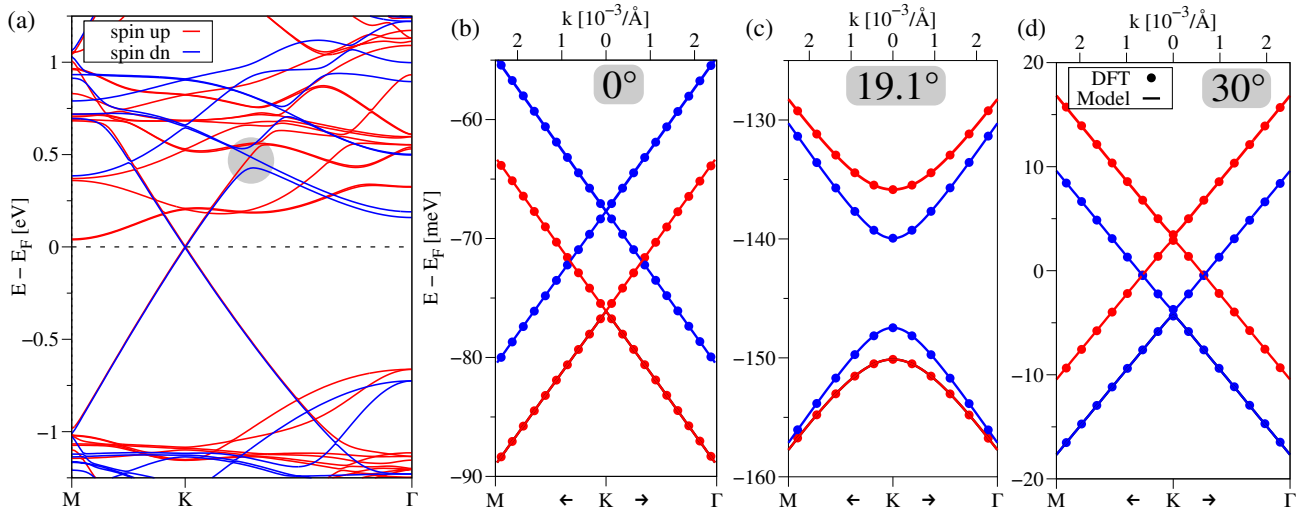

FIG. 2. (a) DFT-calculated band structure of the graphene/CGT heterostructure along the high-symmetry path M-K-Γ for a twist angle of 30°. Red (blue) solid lines correspond to spin up (spin down). Grey disk indicates anticrossing of Dirac and CGT bands. (b) Zoom to the DFT-calculated (symbols) low energy Dirac bands near the K point with a fit to the model Hamiltonian (solid lines) for a twist angle of 0°. (c) and (d) are the same as (b) but for 19.1° and 30°.

4 to −4 meV, when twisting from 0° to 30°. Antiferromagnetic exchange emerges only at 19.1°. Figure 3 also shows data for structures, where only graphene is strained (CGT is kept unstrained), to demonstrate the robustness of these findings against strain; we note that strain controls mainly the band offsets and related charge transfer, see SM [84].

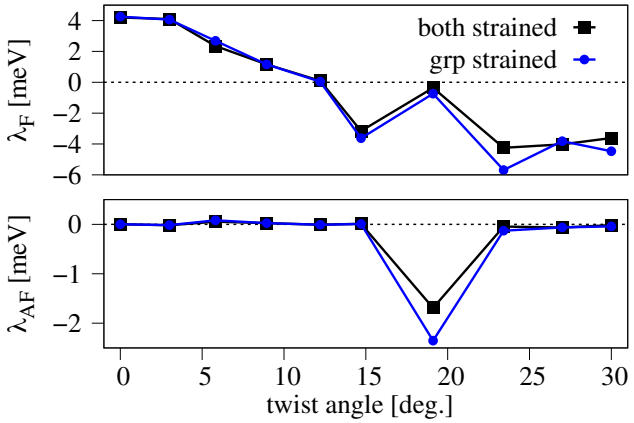

FIG. 3. Calculated twist-angle dependence of the ferromagnetic (top), λ_F, and antiferromagnetic (bottom), λ_{AF}, proximity exchange coupling of the graphene/CGT bilayers. We summarize the results for heterostructures with both layers strained and with only graphene strained.

Tunability by electric field. We now consider the graphene/CGT stacks with different twist angles and apply a transverse electric field between ±1.5 V/nm. The positive direction of the field is indicated in Fig. 1. We wish to answer the question: Can one tune the proximity-induced exchange coupling by gating?

In Fig. 4 we summarize the calculated electric-field and twist-angle dependence of the proximity-induced ferromagnetic and antiferromagnetic exchange coupling, as listed in Table S5. While the qualitative picture of spin-polarization reversal at 30° and appearance of antiferromagnetic polarization at 19.1° remains unchanged, the applied electric field can tune the proximity magnetization rather significantly for some twist angles. A striking example is the 12.2° twist angle: Even though the proximity exchange parameters are small, they can be tuned from positive to negative by the gate field. The antiferromagnetic proximity exchange at 19.1° stays, but is weakly tunable by the field. Overall, we find that both gating and twisting are two efficient knobs to tailor the signs and magnitudes of the proximity-induced exchange couplings in graphene/CGT bilayers. We expect similar tunabilities (although at different twist angles, see below) for other graphene/ferromagnetic-insulator heterostructures.

Sensitivity to interlayer distance and atomic registry. We find that the interlayer distance strongly influences the proximity exchange, see Table S6. Tuning d_{int} by ±0.1 Å, the exchange parameters can be tuned by about ∓30%. Such tunability has recently been measured for the proximity SOC in graphene/WSe_2 heterostructures [69, 87]. The atomic registry does not play a role for proximity exchange couplings for 0° and 30° twist angles. However, as we show in the SM [84], shifting the layers relative to each other, while keeping the twist angle at 19.1°, one can get both staggered and uniform exchange couplings. At this angle the heterostructure supercell is relatively small (24 atoms), making the proximity exchange coupling particularly sensitive to the atomic reg-

istry. Further encapsulation of graphene within two CGT layers provides additional boost and tailoring of proximity exchange, see SM [84].

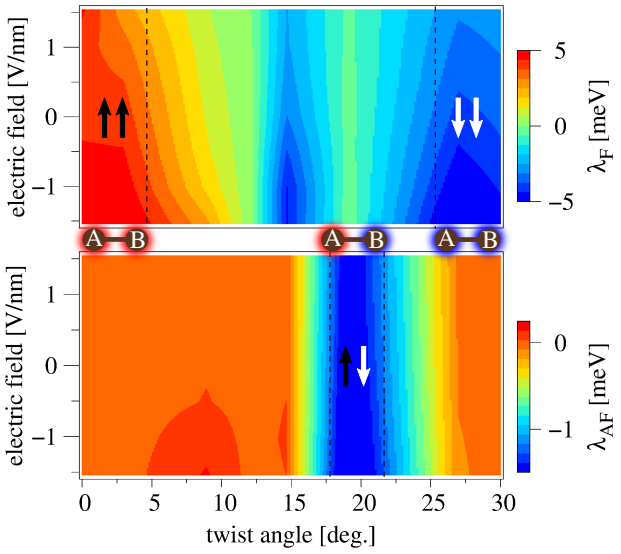

FIG. 4. Calculated electric-field and twist-angle dependence of the ferromagnetic (top), λ_F, and antiferromagnetic (bottom), λ_{AF}, proximity-induced exchange coupling (interpolated from Table S5). Vertical dashed lines indicate regions of strong ferromagnetic/antiferromagnetic exchange. The spin polarizations on the graphene lattice are sketched (see also Fig. 1).

Mechanism of twist-angle dependence of proximity exchange. The Dirac electrons couple to different sets of CGT Bloch states (backfolding) for different twist angles. The first approach to deduce the form of proximity exchange is to look at the relevant CGT energy dispersions with respect to the Dirac point, see Fig. 5. However, this simple picture could be misleading. Second-order perturbation theory predicts that energy levels of coupled states repel. Figure 5 then suggests that for 0° spin up Dirac bands are pushed above spin down bands, and vice versa for 30°. This is in contrast to what is predicted in Fig. 2(b) and (d).

To understand the proximity exchange, one also needs to consider hybridization between the relevant orbitals. Indeed, consider the full band structure presented at Fig. 2(a) for 30°. There is a pronounced anticrossing (grey disk) signalling a particularly strong coupling of spin down carbon p_z orbitals and the lowest CGT spin down conduction band states. This coupling, which is nicely seen in the density plots in Fig. S12 [84], lowers the spin down Dirac states with respect to spin up states, in agreement with Fig. 2(d). Similar observations hold for 0° and 19.1° cases, see SM [84]. However, the complexity of the involved band couplings, due to the necessarily large sizes of the commensurate supercells , limits the power of such qualitative inspections and underscores the need for DFT simulations.

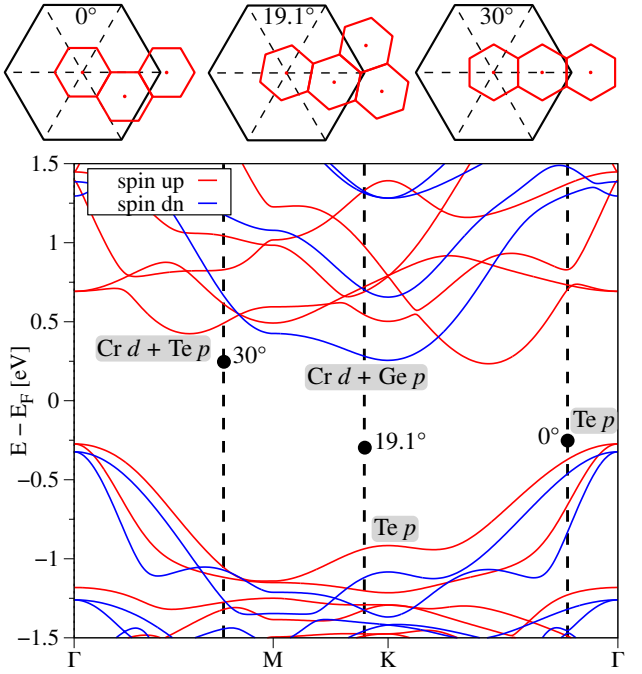

FIG. 5. Top: Backfolding of the graphene Dirac point at K to k points of CGT for different twist angles. The black (red) hexagons represent the graphene (CGT) Brillouin zones. Bottom: The DFT-calculated band structure of monolayer CGT, where the vertical dashed lines indicate the k-points, to which the Dirac states couple to, according to the backfolding. The black dots are the locations of the Dirac point for the different twist angles from Table S4, when CGT is unstrained. We also indicate the main orbital contribution of the bands close to the black dots.

Conclusions. Employing DFT on large supercells we show that one can engineer the proximity exchange of Dirac electrons in graphene/CGT stacks by twisting, which should be useful for spin transport experiments — spin Hanle effect, spin relaxation anisotropy, spin torque — as well as for realizing topological states [40, 88, 89] requiring both SOC and (ferro- or antiferromagnetic) exchange in graphene. Our results also stress the importance of documenting the twist angle when employing magnetic vdW heterostructures in experiments.

This work was funded by the Deutsche Forschungsgemeinschaft (DFG, German Research Foundation) SFB 1277 (Project No. 314695032), SPP 2244 (Project No. 443416183), and the European Union Horizon 2020 Research and Innovation Program under contract number 881603 (Graphene Flagship).

* klaus.zollner@physik.uni-regensburg.de

[1] Stephen Carr, Daniel Massatt, Shiang Fang, Paul Cazeaux, Mitchell Luskin, and Efthimios Kaxiras,

"Twistronics: Manipulating the electronic properties of two-dimensional layered structures through their twist angle," Phys. Rev. B **95**, 075420 (2017).
[2] Zachariah Hennighausen and Swastik Kar, "Twistronics: a turning point in 2d quantum materials," Electronic Structure **3**, 014004 (2021).
[3] Rebeca Ribeiro-Palau, Changjian Zhang, Kenji Watanabe, Takashi Taniguchi, James Hone, and Cory R. Dean, "Twistable electronics with dynamically rotatable heterostructures," Science **361**, 690–693 (2018).
[4] Stephen Carr, Shiang Fang, and Efthimios Kaxiras, "Electronic-structure methods for twisted moiré layers," Nature Reviews Materials **5**, 748–763 (2020).
[5] Yuan Cao, Valla Fatemi, Shiang Fang, Kenji Watanabe, Takashi Taniguchi, Efthimios Kaxiras, and Pablo Jarillo-Herrero, "Unconventional superconductivity in magic-angle graphene superlattices," Nature **556**, 43 (2018).
[6] Yuan Cao, Valla Fatemi, Ahmet Demir, Shiang Fang, Spencer L. Tomarken, Jason Y. Luo, Javier D. Sanchez-Yamagishi, Kenji Watanabe, Takashi Taniguchi, Efthimios Kaxiras, Ray C. Ashoori, and Pablo Jarillo-Herrero, "Correlated insulator behaviour at half-filling in magic-angle graphene superlattices," Nature **556**, 80 (2018).
[7] Harpreet Singh Arora, Robert Polski, Yiran Zhang, Alex Thomson, Youngjoon Choi, Hyunjin Kim, Zhong Lin, Ilham Zaky Wilson, Xiaodong Xu, Jiun-Haw Chu, *et al.*, "Superconductivity in metallic twisted bilayer graphene stabilized by wse 2," Nature **583**, 379–384 (2020).
[8] Petr Stepanov, Ipsita Das, Xiaobo Lu, Ali Fahimniya, Kenji Watanabe, Takashi Taniguchi, Frank HL Koppens, Johannes Lischner, Leonid Levitov, and Dmitri K Efetov, "Untying the insulating and superconducting orders in magic-angle graphene," Nature **583**, 375–378 (2020).
[9] Xiaobo Lu, Petr Stepanov, Wei Yang, Ming Xie, Mohammed Ali Aamir, Ipsita Das, Carles Urgell, Kenji Watanabe, Takashi Taniguchi, Guangyu Zhang, *et al.*, "Superconductors, orbital magnets and correlated states in magic-angle bilayer graphene," Nature **574**, 653–657 (2019).
[10] Aaron L. Sharpe, Eli J. Fox, Arthur W. Barnard, Joe Finney, Kenji Watanabe, Takashi Taniguchi, M. A. Kastner, and David Goldhaber-Gordon, "Emergent ferromagnetism near three-quarters filling in twisted bilayer graphene," Science **365**, 605–608 (2019).
[11] Yu Saito, Fangyuan Yang, Jingyuan Ge, Xiaoxue Liu, Takashi Taniguchi, Kenji Watanabe, JIA Li, Erez Berg, and Andrea F Young, "Isospin pomeranchuk effect in twisted bilayer graphene," Nature **592**, 220–224 (2021).
[12] M. Serlin, C. L. Tschirhart, H. Polshyn, Y. Zhang, J. Zhu, K. Watanabe, T. Taniguchi, L. Balents, and A. F. Young, "Intrinsic quantized anomalous hall effect in a moire heterostructure," Science **367**, 900–903 (2020).
[13] Amol Nimbalkar and Hyunmin Kim, "Opportunities and challenges in twisted bilayer graphene: a review," Nano-Micro Letters **12**, 126 (2020).
[14] Nick Bultinck, Shubhayu Chatterjee, and Michael P. Zaletel, "Mechanism for anomalous hall ferromagnetism in twisted bilayer graphene," Phys. Rev. Lett. **124**, 166601 (2020).
[15] Cécile Repellin, Zhihuan Dong, Ya-Hui Zhang, and T. Senthil, "Ferromagnetism in narrow bands of moiré superlattices," Phys. Rev. Lett. **124**, 187601 (2020).
[16] Youngjoon Choi, Jeannette Kemmer, Yang Peng, Alex Thomson, Harpreet Arora, Robert Polski, Yiran Zhang, Hechen Ren, Jason Alicea, Gil Refael, *et al.*, "Electronic correlations in twisted bilayer graphene near the magic angle," Nature Physics **15**, 1174–1180 (2019).
[17] Simone Lisi, Xiaobo Lu, Tjerk Benschop, Tobias A de Jong, Petr Stepanov, Jose R Duran, Florian Margot, Irène Cucchi, Edoardo Cappelli, Andrew Hunter, *et al.*, "Observation of flat bands in twisted bilayer graphene," Nature Physics **17**, 189–193 (2021).
[18] Leon Balents, Cory R Dean, Dmitri K Efetov, and Andrea F Young, "Superconductivity and strong correlations in moiré flat bands," Nature Physics **16**, 725–733 (2020).
[19] T. M. R. Wolf, J. L. Lado, G. Blatter, and O. Zilberberg, "Electrically tunable flat bands and magnetism in twisted bilayer graphene," Phys. Rev. Lett. **123**, 096802 (2019).
[20] Ziyan Zhu, Stephen Carr, Daniel Massatt, Mitchell Luskin, and Efthimios Kaxiras, "Twisted trilayer graphene: A precisely tunable platform for correlated electrons," Phys. Rev. Lett. **125**, 116404 (2020).
[21] Jeong Min Park, Yuan Cao, Kenji Watanabe, Takashi Taniguchi, and Pablo Jarillo-Herrero, "Tunable strongly coupled superconductivity in magic-angle twisted trilayer graphene," Nature **590**, 249–255 (2021).
[22] Guorui Chen, Lili Jiang, Shuang Wu, Bosai Lyu, Hongyuan Li, Bheema Lingam Chittari, Kenji Watanabe, Takashi Taniguchi, Zhiwen Shi, Jeil Jung, *et al.*, "Evidence of a gate-tunable mott insulator in a trilayer graphene moiré superlattice," Nature Physics **15**, 237–241 (2019).
[23] Guorui Chen, Aaron L Sharpe, Eli J Fox, Ya-Hui Zhang, Shaoxin Wang, Lili Jiang, Bosai Lyu, Hongyuan Li, Kenji Watanabe, Takashi Taniguchi, *et al.*, "Tunable correlated chern insulator and ferromagnetism in a moiré superlattice," Nature **579**, 56–61 (2020).
[24] Guorui Chen, Aaron L Sharpe, Patrick Gallagher, Ilan T Rosen, Eli J Fox, Lili Jiang, Bosai Lyu, Hongyuan Li, Kenji Watanabe, Takashi Taniguchi, *et al.*, "Signatures of tunable superconductivity in a trilayer graphene moiré superlattice," Nature **572**, 215–219 (2019).
[25] Haoxin Zhou, Tian Xie, Areg Ghazaryan, Tobias Holder, James R. Ehrets, Eric M. Spanton, Takashi Taniguchi, Kenji Watanabe, Erez Berg, Maksym Serbyn, and Andrea F. Young, "Half and quarter metals in rhombohedral trilayer graphene," arXiv:2104.00653 (2021).
[26] Yang-Zhi Chou, Fengcheng Wu, Jay D. Sau, and Sankar Das Sarma, "Acoustic-phonon-mediated superconductivity in rhombohedral trilayer graphene," arXiv:2106.13231 (2021).
[27] Vo Tien Phong, Pierre A. Pantaleón, Tommaso Cea, and Francisco Guinea, "Band structure and superconductivity in twisted trilayer graphene," arXiv:2106.15573 (2021).
[28] Haoxin Zhou, Tian Xie, Takashi Taniguchi, Kenji Watanabe, and Andrea F. Young, "Superconductivity in rhombohedral trilayer graphene," arXiv:2106.07640 (2021).

[29] Wei Qin and Allan H. MacDonald, "In-plane critical magnetic fields in magic-angle twisted trilayer graphene," arXiv:2104.14026 (2021).

[30] Yanhao Tang, Lizhong Li, Tingxin Li, Yang Xu, Song Liu, Katayun Barmak, Kenji Watanabe, Takashi Taniguchi, Allan H MacDonald, Jie Shan, *et al.*, "Simulation of hubbard model physics in wse 2/ws 2 moiré superlattices," Nature **579**, 353–358 (2020).

[31] Juan F Sierra, Jaroslav Fabian, Roland K Kawakami, Stephan Roche, and Sergio O Valenzuela, "Van der waals heterostructures for spintronics and opto-spintronics," Nature Nanotechnology , 1–13 (2021).

[32] Rai Moriya, Naoto Yabuki, and Tomoki Machida, "Superconducting proximity effect in a $Nbse_2$/graphene van der waals junction," Phys. Rev. B **101**, 054503 (2020).

[33] Hui Han, Jie Ling, Wenhui Liu, Hui Li, Changjin Zhang, and Jiannong Wang, "Superconducting proximity effect in a van der waals 2h-tas2/nbse2 heterostructure," Applied Physics Letters **118**, 253101 (2021).

[34] Klaus Zollner, Martin Gmitra, Tobias Frank, and Jaroslav Fabian, "Theory of proximity-induced exchange coupling in graphene on hbn/(co, ni)," Phys. Rev. B **94**, 155441 (2016).

[35] Klaus Zollner, Martin Gmitra, and Jaroslav Fabian, "Electrically tunable exchange splitting in bilayer graphene on monolayer Cr 2 X 2 Te 6 with X = Ge, Si, and Sn," New J. Phys. **20**, 073007 (2018).

[36] Klaus Zollner, Paulo E. Faria Junior, and Jaroslav Fabian, "Proximity exchange effects in $mose_2$ and wse_2 heterostructures with cri_3: Twist angle, layer, and gate dependence," Phys. Rev. B **100**, 085128 (2019).

[37] Klaus Zollner, Paulo E. Faria Junior, and Jaroslav Fabian, "Giant proximity exchange and valley splitting in transition metal dichalcogenide/hBN/(co, ni) heterostructures," Phys. Rev. B **101**, 085112 (2020).

[38] Ali Hallal, Fatima Ibrahim, Hongxin Yang, Stephan Roche, and Mairbek Chshiev, "Tailoring magnetic insulator proximity effects in graphene: first-principles calculations," 2D Mater. **4**, 025074 (2017).

[39] Jiayong Zhang, Bao Zhao, Yugui Yao, and Zhongqin Yang, "Robust quantum anomalous hall effect in graphene-based van der waals heterostructures," Phys. Rev. B **92**, 165418 (2015).

[40] Jiayong Zhang, Bao Zhao, Tong Zhou, Yang Xue, Chunlan Ma, and Zhongqin Yang, "Strong magnetization and Chern insulators in compressed graphene/CrI_3 van der Waals heterostructures," Phys. Rev. B **97**, 085401 (2018).

[41] H. X. Yang, A. Hallal, D. Terrade, X. Waintal, S. Roche, and M. Chshiev, "Proximity effects induced in graphene by magnetic insulators: First-principles calculations on spin filtering and exchange-splitting gaps," Phys. Rev. Lett. **110**, 046603 (2013).

[42] A Dyrdał and J Barnaś, "Anomalous, spin, and valley hall effects in graphene deposited on ferromagnetic substrates," 2D Mater. **4**, 034003 (2017).

[43] Yu Song, "Electric-field-induced extremely large change in resistance in graphene ferromagnets," J. Phys. D: Appl. Phys. **51**, 025002 (2018).

[44] Håvard Haugen, Daniel Huertas-Hernando, and Arne Brataas, "Spin transport in proximity-induced ferromagnetic graphene," Phys. Rev. B **77**, 115406 (2008).

[45] Jiayong Zhang, Bao Zhao, Yugui Yao, and Zhongqin Yang, "Quantum Anomalous Hall Effect in Graphene-based Heterostructure," Sci. Rep. **5**, 10629 (2015).

[46] Shanshan Su, Yafis Barlas, Junxue Li, Jing Shi, and Roger K. Lake, "Effect of intervalley interaction on band topology of commensurate graphene/euo heterostructures," Phys. Rev. B **95**, 075418 (2017).

[47] M. Gibertini, M. Koperski, A. F. Morpurgo, and K. S. Novoselov, "Magnetic 2D materials and heterostructures," Nat. Nanotechnol. **14**, 408 (2019).

[48] D. R. Klein, D. MacNeill, J. L. Lado, D. Soriano, E. Navarro-Moratalla, K. Watanabe, T. Taniguchi, S. Manni, P. Canfield, J. Fernández-Rossier, and P. Jarillo-Herrero, "Probing magnetism in 2D van der Waals crystalline insulators via electron tunneling," Science **360**, 1218 (2018).

[49] C. Cardoso, D. Soriano, N. A. García-Martínez, and J. Fernández-Rossier, "Van der waals spin valves," Phys. Rev. Lett. **121**, 067701 (2018).

[50] J. C. G. Henriques, G. Catarina, A. T. Costa, J. Fernández-Rossier, and N. M. R. Peres, "Excitonic magneto-optical kerr effect in two-dimensional transition metal dichalcogenides induced by spin proximity," Phys. Rev. B **101**, 045408 (2020).

[51] Simranjeet Singh, Jyoti Katoch, Tiancong Zhu, Keng Yuan Meng, Tianyu Liu, Jack T. Brangham, Fengyuan Yang, Michael E. Flatté, and Roland K. Kawakami, "Strong Modulation of Spin Currents in Bilayer Graphene by Static and Fluctuating Proximity Exchange Fields," Phys. Rev. Lett. **118**, 187201 (2017).

[52] Adrian G. Swartz, Patrick M. Odenthal, Yufeng Hao, Rodney S. Ruoff, and Roland K. Kawakami, "Integration of the ferromagnetic insulator EuO onto graphene," ACS Nano **6**, 10063 (2012).

[53] Martin Gmitra and Jaroslav Fabian, "Graphene on transition-metal dichalcogenides: A platform for proximity spin-orbit physics and optospintronics," Phys. Rev. B **92**, 155403 (2015).

[54] Martin Gmitra, Denis Kochan, Petra Högl, and Jaroslav Fabian, "Trivial and inverted dirac bands and the emergence of quantum spin hall states in graphene on transition-metal dichalcogenides," Phys. Rev. B **93**, 155104 (2016).

[55] Klaus Zollner and Jaroslav Fabian, "Single and bilayer graphene on the topological insulator bi_2se_3: Electronic and spin-orbit properties from first principles," Phys. Rev. B **100**, 165141 (2019).

[56] Klaus Zollner and Jaroslav Fabian, "Heterostructures of graphene and topological insulators bi2se3, bi2te3, and sb2te3," physica status solidi (b) **258**, 2000081 (2021).

[57] Dmitrii Khokhriakov, Anamul Md. Hoque, Bogdan Karpiak, and Saroj P. Dash, "Gate-tunable spin-galvanic effect in graphene-topological insulator van der waals heterostructures at room temperature," Nature Communications **11** (2020), 10.1038/s41467-020-17481-1.

[58] Bogdan Karpiak, Aron W. Cummings, Klaus Zollner, Marc Vila, Dmitrii Khokhriakov, Anamul Md Hoque, André Dankert, Peter Svedlindh, Jaroslav Fabian, Stephan Roche, and Saroj P. Dash, "Magnetic proximity in a van der Waals heterostructure of magnetic insulator and graphene," 2D Mater. **7**, 015026 (2019).

[59] Simon Zihlmann, Aron W. Cummings, Jose H. Garcia, Máté Kedves, Kenji Watanabe, Takashi Taniguchi, Christian Schönenberger, and Péter Makk, "Large spin relaxation anisotropy and valley-zeeman spin-orbit cou-

pling in wse_2/graphene/h-bn heterostructures," Phys. Rev. B **97**, 075434 (2018).
[60] Kenan Song, David Soriano, Aron W. Cummings, Roberto Robles, Pablo Ordejón, and Stephan Roche, "Spin Proximity Effects in Graphene/Topological Insulator Heterostructures," Nano Lett. **18**, 2033 (2018).
[61] Dmitrii Khokhriakov, Aron W. Cummings, Kenan Song, Marc Vila, Bogdan Karpiak, André Dankert, Stephan Roche, and Saroj P. Dash, "Tailoring emergent spin phenomena in Dirac material heterostructures," Sci. Adv. **4**, eaat9349 (2018).
[62] Jose H. Garcia, Marc Vila, Aron W. Cummings, and Stephan Roche, "Spin transport in graphene/transition metal dichalcogenide heterostructures," Chem. Soc. Rev. **47**, 3359 (2018).
[63] CK Safeer, Josep Ingla-Aynés, Franz Herling, José H Garcia, Marc Vila, Nerea Ontoso, M Reyes Calvo, Stephan Roche, Luis E Hueso, and Fèlix Casanova, "Room-temperature spin Hall effect in graphene/MoS_2 van der Waals heterostructures," Nano Lett. **19**, 1074 (2019).
[64] Franz Herling, C. K. Safeer, Josep Ingla-Aynés, Nerea Ontoso, Luis E. Hueso, and Fèlix Casanova, "Gate tunability of highly efficient spin-to-charge conversion by spin hall effect in graphene proximitized with wse2," APL Materials **8**, 071103 (2020).
[65] Jun Yong Khoo, Alberto F. Morpurgo, and Leonid Levitov, "On-Demand Spin-Orbit Interaction from Which-Layer Tunability in Bilayer Graphene," Nano Lett. **17**, 7003 (2017).
[66] Zhe Wang, Dong-Keun Ki, Hua Chen, Helmuth Berger, Allan H MacDonald, and Alberto F Morpurgo, "Strong interface-induced spin-orbit interaction in graphene on WS2," Nat. Commun. **6**, 8339 (2015).
[67] S. Omar and B. J. van Wees, "Spin transport in high-mobility graphene on ws_2 substrate with electric-field tunable proximity spin-orbit interaction," Phys. Rev. B **97**, 045414 (2018).
[68] S. Omar and B. J. van Wees, "Graphene-ws_2 heterostructures for tunable spin injection and spin transport," Phys. Rev. B **95**, 081404 (2017).
[69] Balint Fülöp, Albin Marffy, Simon Zihlmann, Martin Gmitra, Endre Tovari, Balint Szentpeteri, Mate Kedves, Kenji Watanabe, Takashi Taniguchi, Jaroslav Fabian, Christian Schönenberger, Peter Makk, and Szabolcs Csonka, "Boosting proximity spin orbit coupling in graphene/wse_2 heterostructures via hydrostatic pressure," arXiv:2103.13325 (2021).
[70] Klaus Zollner, Marko D. Petrović, Kapildeb Dolui, Petr Plecháč, Branislav K. Nikolić, and Jaroslav Fabian, "Scattering-induced and highly tunable by gate damping-like spin-orbit torque in graphene doubly proximitized by two-dimensional magnet $cr_2ge_2te_6$ and monolayer ws_2," Phys. Rev. Research **2**, 043057 (2020).
[71] M Umar Farooq and Jisang Hong, "Switchable valley splitting by external electric field effect in graphene/cri 3 heterostructures," npj 2D Materials and Applications **3**, 1–7 (2019).
[72] Kyle L. Seyler, Ding Zhong, Bevin Huang, Xiayu Linpeng, Nathan P. Wilson, Takashi Taniguchi, Kenji Watanabe, Wang Yao, Di Xiao, Michael A. McGuire, Kai-Mei C. Fu, and Xiaodong Xu, "Valley Manipulation by Optically Tuning the Magnetic Proximity Effect in WSe 2 /CrI 3 Heterostructures," Nano Lett. **18**, 3823 (2018).
[73] Zhiyong Wang, Chi Tang, Raymond Sachs, Yafis Barlas, and Jing Shi, "Proximity-induced ferromagnetism in graphene revealed by the anomalous hall effect," Phys. Rev. Lett. **114**, 016603 (2015).
[74] J. B. S. Mendes, O. Alves Santos, L. M. Meireles, R. G. Lacerda, L. H. Vilela-Leão, F. L. A. Machado, R. L. Rodríguez-Suárez, A. Azevedo, and S. M. Rezende, "Spin-Current to Charge-Current Conversion and Magnetoresistance in a Hybrid Structure of Graphene and Yttrium Iron Garnet," Phys. Rev. Lett. **115**, 226601 (2015).
[75] Johannes Christian Leutenantsmeyer, Alexey A Kaverzin, Magdalena Wojtaszek, and Bart J van Wees, "Proximity induced room temperature ferromagnetism in graphene probed with spin currents," 2D Mater. **4**, 014001 (2016).
[76] Klaus Zollner, Martin Gmitra, and Jaroslav Fabian, "Swapping exchange and spin-orbit coupling in 2d van der waals heterostructures," Phys. Rev. Lett. **125**, 196402 (2020).
[77] Kapildeb Dolui, Marko D Petrovic, Klaus Zollner, Petr Plechac, Jaroslav Fabian, and Branislav K Nikolic, "Proximity spin–orbit torque on a two-dimensional magnet within van der waals heterostructure: current-driven antiferromagnet-to-ferromagnet reversible nonequilibrium phase transition in bilayer cri3," Nano letters **20**, 2288–2295 (2020).
[78] Mohammed Alghamdi, Mark Lohmann, Junxue Li, Palani R Jothi, Qiming Shao, Mohammed Aldosary, Tang Su, Boniface P. T. Fokwa, and Jing Shi, "Highly Efficient Spin–Orbit Torque and Switching of Layered Ferromagnet Fe 3 GeTe 2," Nano Lett. **19**, 4400 (2019).
[79] Xiao Wang, Jian Tang, Xiuxin Xia, Congli He, Junwei Zhang, Yizhou Liu, Caihua Wan, Chi Fang, Chenyang Guo, Wenlong Yang, Yao Guang, Xiaomin Zhang, Hongjun Xu, Jinwu Wei, Mengzhou Liao, Xiaobo Lu, Jiafeng Feng, Xiaoxi Li, Yong Peng, Hongxiang Wei, Rong Yang, Dongxia Shi, Xixiang Zhang, Zheng Han, Zhidong Zhang, Guangyu Zhang, Guoqiang Yu, and Xiufeng Han, "Current-driven magnetization switching in a van der waals ferromagnet fe3gete2," Science Advances **5** (2019), 10.1126/sciadv.aaw8904.
[80] Predrag Lazić, K. D. Belashchenko, and Igor Žutić, "Effective gating and tunable magnetic proximity effects in two-dimensional heterostructures," Phys. Rev. B **93**, 241401 (2016).
[81] Shiming Yan, Shengmei Qi, Dunhui Wang, and Wenbo Mi, "Novel electronic structures and magnetic properties in twisted two-dimensional graphene/janus 2h–vsete heterostructures," Physica E: Low-dimensional Systems and Nanostructures **134**, 114854 (2021).
[82] Alessandro David, Péter Rakyta, Andor Kormányos, and Guido Burkard, "Induced spin-orbit coupling in twisted graphene–transition metal dichalcogenide heterobilayers: Twistronics meets spintronics," Phys. Rev. B **100**, 085412 (2019).
[83] Yang Li and Mikito Koshino, "Twist-angle dependence of the proximity spin-orbit coupling in graphene on transition-metal dichalcogenides," Phys. Rev. B **99**, 075438 (2019).
[84] See Supplemental Material, including Refs. [4, 34, 39, 58, 69, 70, 75, 82, 83, 87, 88, 90–108] where we show a

more extended summary of results.
[85] Denis Kochan, Susanne Irmer, and Jaroslav Fabian, "Model spin-orbit coupling hamiltonians for graphene systems," Phys. Rev. B **95**, 165415 (2017).
[86] Võ Tien Phong, Niels R Walet, and Francisco Guinea, "Effective interactions in a graphene layer induced by the proximity to a ferromagnet," 2D Mater. **5**, 014004 (2017).
[87] Balint Fülöp, Albin Marffy, Endre Tovari, Mate Kedves, Simon Zihlmann, David Indolese, Zoltan Kovacs-Krausz, Kenji Watanabe, Takashi Taniguchi, Christian Schönenberger, Istvan Kezsmarki, Peter Makk, and Szabolcs Csonka, "Transport measurements on van der waals heterostructures under pressure," arXiv:2103.14617 (2021).
[88] Petra Högl, Tobias Frank, Klaus Zollner, Denis Kochan, Martin Gmitra, and Jaroslav Fabian, "Quantum anomalous hall effects in graphene from proximity-induced uniform and staggered spin-orbit and exchange coupling," Phys. Rev. Lett. **124**, 136403 (2020).
[89] Marc Vila, Jose H. Garcia, and Stephan Roche, "Valley-polarized quantum anomalous hall phase in bilayer graphene with layer-dependent proximity effects," arXiv:2107.00034 (2021).
[90] S. R. Bahn and K. W. Jacobsen, "An object-oriented scripting interface to a legacy electronic structure code," Comput. Sci. Eng. **4**, 56 (2002).
[91] Predrag Lazic, "Cellmatch: Combining two unit cells into a common supercell with minimal strain," Computer Physics Communications **197**, 324 – 334 (2015).
[92] Daniel S Koda, Friedhelm Bechstedt, Marcelo Marques, and Lara K Teles, "Coincidence lattices of 2d crystals: heterostructure predictions and applications," The Journal of Physical Chemistry C **120**, 10895–10908 (2016).
[93] Y. Baskin and L. Meyer, "Lattice constants of graphite at low temperatures," Phys. Rev. **100**, 544 (1955).
[94] V Carteaux, D Brunet, G Ouvrard, and G Andre, "Crystallographic, magnetic and electronic structures of a new layered ferromagnetic compound Cr2Ge2Te6," J. Phys.: Condens. Mat. **7**, 69 (1995).
[95] P. Hohenberg and W. Kohn, "Inhomogeneous electron gas," Phys. Rev. **136**, B864 (1964).
[96] Paolo Giannozzi and et al., "Quantum espresso: a modular and open-source software project for quantum simulations of materials," J. Phys.: Cond. Mat. **21**, 395502 (2009).
[97] Cheng Gong, Lin Li, Zhenglu Li, Huiwen Ji, Alex Stern, Yang Xia, Ting Cao, Wei Bao, Chenzhe Wang, Yuan Wang, Z. Q. Qiu, R. J. Cava, Steven G. Louie, Jing Xia, and Xiang Zhang, "Discovery of intrinsic ferromagnetism in two-dimensional van der Waals crystals," Nature **546**, 265 (2017).
[98] G. Kresse and D. Joubert, "From ultrasoft pseudopotentials to the projector augmented-wave method," Phys. Rev. B **59**, 1758 (1999).
[99] John P. Perdew, Kieron Burke, and Matthias Ernzerhof, "Generalized gradient approximation made simple," Phys. Rev. Lett. **77**, 3865 (1996).
[100] Stefan Grimme, "Semiempirical gga-type density functional constructed with a long-range dispersion correction," J. Comput. Chem. **27**, 1787 (2006).
[101] Stefan Grimme, Jens Antony, Stephan Ehrlich, and Helge Krieg, "A consistent and accurate ab initio parametrization of density functional dispersion correction (DFT-D) for the 94 elements H-Pu," J. Chem. Phys. **132**, 154104 (2010).
[102] Vincenzo Barone, Maurizio Casarin, Daniel Forrer, Michele Pavone, Mauro Sambi, and Andrea Vittadini, "Role and effective treatment of dispersive forces in materials: Polyethylene and graphite crystals as test cases," J. Comput. Chem. **30**, 934 (2009).
[103] Lennart Bengtsson, "Dipole correction for surface supercell calculations," Phys. Rev. B **59**, 12301 (1999).
[104] Xingxing Li and Jinlong Yang, "CrXTe 3 (X = Si, Ge) nanosheets: two dimensional intrinsic ferromagnetic semiconductors," J. Mater. Chem. C **2**, 7071 (2014).
[105] Xiaofang Chen, Jingshan Qi, and Daning Shi, "Strain-engineering of magnetic coupling in two-dimensional magnetic semiconductor crsite3: Competition of direct exchange interaction and superexchange interaction," Phys. Letters A **379**, 60 (2015).
[106] Talieh S. Ghiasi, Alexey A. Kaverzin, Avalon H. Dismukes, Dennis K. de Wal, Xavier Roy, and Bart J. van Wees, "Electrical and thermal generation of spin currents by magnetic bilayer graphene," Nature Nanotechnology (2021), 10.1038/s41565-021-00887-3.
[107] Tribhuwan Pandey, Avinash P. Nayak, Jin Liu, Samuel T. Moran, Joon-Seok Kim, Lain-Jong Li, Jung-Fu Lin, Deji Akinwande, and Abhishek K. Singh, "Pressure-induced charge transfer doping of monolayer graphene/mos2 heterostructure," Small **12**, 4063–4069 (2016).
[108] Klaus Zollner and Jaroslav Fabian, "Bilayer graphene encapsulated within monolayers of ws_2 or $cr_2ge_2te_6$: Tunable proximity spin-orbit or exchange coupling," arXiv:2103.15378 (2021).

Supplemental Material: Engineering proximity exchange by twisting: Reversal of ferromagnetic and emergence of antiferromagnetic Dirac bands in graphene/$Cr_2Ge_2Te_6$

Klaus Zollner[1] and Jaroslav Fabian[1]

[1]*Institute for Theoretical Physics, University of Regensburg, 93040 Regensburg, Germany*

In the Supplemental Material, we give a more extended summary of our results from the main text. First, we give a description of the computational details, the geometry setup, and structural information. Next, we show the band structure and fit results for three most relevant twist angles, 0, 19.1, and 30 degrees. For all angles, we summarize the fit parameters in tabular form. After that, we discuss the influence of in-plane strain on the results. For this second set of structures, where $Cr_2Ge_2Te_6$ (CGT) is unstrained, we also summarize the structural information, fitted parameters, and show band structures and model fits. For the electric field study, we summarize all fit parameters in tabular form, and plot the two sublattice-resolved proximity exchange parameters as function of twist angle and gate field. Similarly, the results for laterally and vertically shifting the graphene with respect to the CGT are also summarized in tabular form. In addition, we briefly discuss CGT encapsulated heterostructures and how one can further tailor proximity exchange in graphene. Finally, we extensively discuss the origin of the different proximity exchange couplings, from the calculated density of states, spin polarizations, projected band structures, as well as from the backfolding of the Dirac states into the CGT Brillouin zone, for different twist angles.

I. COMPUTATIONAL DETAILS AND GEOMETRY

The heterostructures of graphene and CGT, where we consider several twist angles between the two monolayers, are set-up with the `atomic simulation environment (ASE)` [1] and the `CellMatch` code [2], implementing the Coincidence lattice method [3, 4]. Monolayers of graphene and CGT are based on hexagonal unit cells, with lattice constants of $a = 2.46$ Å [5] and 6.8275 Å [6], which need to be strained in the twisted heterostructures, in order to form commensurate supercells for periodic density functional theory (DFT) calculations. In Table S1 we summarize the main structural information for the twist angles we consider. In total, we investigate 10 different angles between 0° and 30°. Especially these angles are suitable for DFT calculations, since strain applied to the monolayers is at maximum 5% and the number of atoms in the supercells is still manageable. Otherwise, also other angles could be investigated, but beyond reasonable strain limits and above 300 atoms in the structure.

TABLE S1. Structural information for the graphene/CGT heterostructures. We list the twist angle between the layers, the number of atoms (NoA) in the heterostructure supercell, the number n_k for the k-point sampling, the lattice constants of graphene and CGT, the calculated dipole of the structure, the relaxed interlayer distance $d_{\rm int}$, the rippling of the graphene layer $\Delta z_{\rm grp}$, and the averaged calculated magnetic moments of Cr, Ge, Te, and C atoms.

twist angle [°]	NoA	n_k	$a_{\rm grp}$ [Å]	$a_{\rm CGT}$ [Å]	dipole [debye]	$d_{\rm int}$ [Å]	$\Delta z_{\rm grp}$ [pm]	Cr [$\mu_{\rm B}$]	Ge [$\mu_{\rm B}$]	Te [$\mu_{\rm B}$]	C [$10^{-3}\mu_{\rm B}$]
0.0000	218	9	2.52	6.718	-2.5453	3.5685	0.554	3.110	0.0213	-0.0817	-0.247
3.0045	302	6	2.48	6.826	-4.4864	3.5303	0.545	3.139	0.0247	-0.0870	-0.132
5.8175	236	9	2.45	6.974	-3.5160	3.5575	0.400	3.191	0.0282	-0.0967	-0.137
8.9483	102	24	2.46	6.848	-1.5072	3.5473	0.613	3.148	0.0251	-0.0886	-0.200
12.2163	224	9	2.50	6.821	-3.1757	3.5619	0.561	3.140	0.0244	-0.0869	-0.214
14.7047	314	6	2.45	6.963	-4.9073	3.5435	0.838	3.186	0.0279	-0.0957	-0.279
19.1066	24	42	2.52	6.663	-0.2338	3.5735	0.392	3.097	0.0194	-0.0797	-0.200
23.4132	242	9	2.45	7.108	-4.0642	3.5372	0.653	3.236	0.0310	-0.1058	-0.240
26.9955	174	12	2.50	6.814	-2.5319	3.5632	0.654	3.138	0.0241	-0.0864	-0.236
30.0000	80	30	2.45	7.073	-1.3044	3.5450	0.918	3.224	0.0301	-0.1033	-0.184

The electronic structure calculations and structural relaxation of graphene/CGT heterostructures are performed by DFT [7] with `Quantum ESPRESSO` [8]. Self-consistent calculations are carried out with a k-point sampling of $n_k \times n_k \times 1$. The number n_k is listed in Table S1 for all twist angles and depends on the number of atoms in the heterostructure. In addition, n_k is limited by our computational power. Nevertheless, for large supercells the heterostructure Brillouin Zone is small and only few k-points are necessary to get converged results.

We perform open shell calculations that provide the spin-polarized ground state of the CGT monolayer. A Hubbard parameter of $U = 1.0$ eV is used for Cr d-orbitals, being in the range of proposed U values for CGT [9]. We use

an energy cutoff for charge density of 520 Ry and the kinetic energy cutoff for wavefunctions is 65 Ry for the scalar relativistic pseudopotential with the projector augmented wave method [10] with the Perdew-Burke-Ernzerhof exchange correlation functional [11]. Spin-orbit coupling (SOC) is neglected, since we are mainly interested in the twist-angle dependent proximity-induced exchange coupling. Moreover, recent calculations have already shown that proximity-induced SOC in graphene, originating from the CGT, is small compared to the exchange coupling [12–14]. For the relaxation of the heterostructures, we add van der Waals (vdW) corrections [15–17] and use quasi-Newton algorithm based on trust radius procedure. Dipole corrections [18] are also included to get correct band offsets and internal electric fields. In order to simulate quasi-2D systems, we add a vacuum of about 24 Å to avoid interactions between periodic images in our slab geometry. To determine the interlayer distances, the atoms of graphene are allowed to relax only along z-direction (vertical to the layers) and the atoms of CGT are allowed to move in all directions, until every component of each force is reduced below 10^{-3} [Ry/a_0], where a_0 is the Bohr radius.

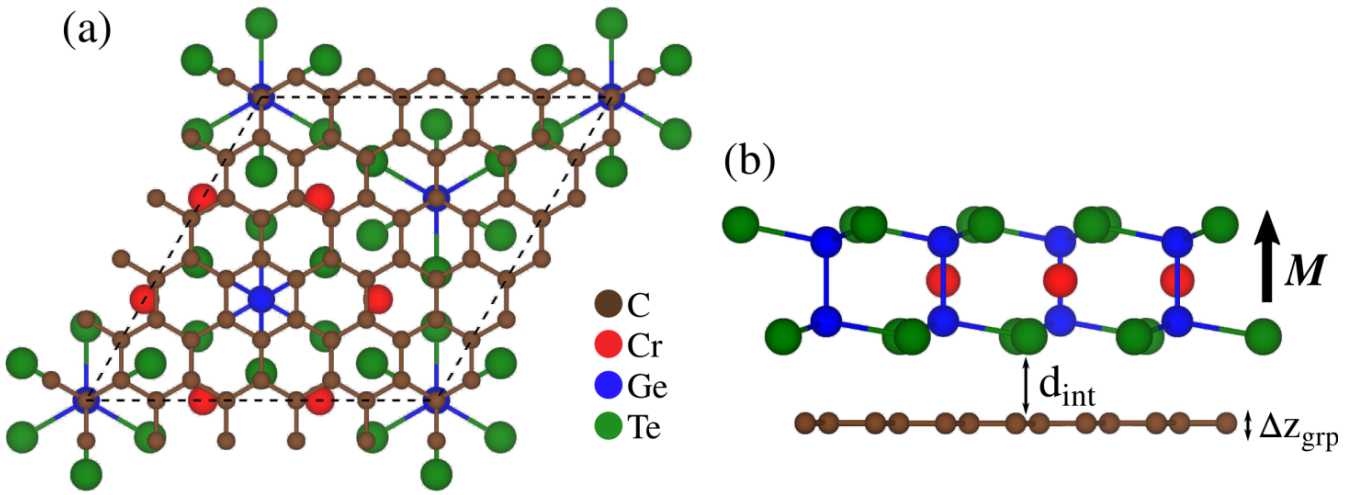

FIG. S1. (a,b) Bottom and side view of the graphene/CGT heterostructure with a twist angle of 30°. Dashed line in (a) defines the heterostructure unit cell and in (b) we define the interlayer distance d_{int} and the rippling of the graphene layer Δz_{grp}. Different colors correspond to different atom types. In all our heterostructures, the CGT layer (with magnetization $\boldsymbol{M}$ along z direction) is above graphene.

After relaxation of the graphene/CGT heterostructures, we calculate the mean interlayer distances, d_{int}, and the standard deviations, Δz_{grp}, from the z coordinates of the C atoms of graphene. The standard deviations represent the amount of rippling of graphene. The results are summarized in Table S1. The interlayer distance is nearly independent of the twist angle and is about 3.55 Å. The graphene itself stays nearly flat, as the rippling is always below 1 pm. In Fig. S1, we show an exemplary case of the graphene/CGT heterostructure for a twist angle of 30°. All our heterostructures have the CGT layer above graphene, with the CGT magnetization $\boldsymbol{M}$ along z direction, specifying the spin quantization axis (spin up = z, spin down = $-z$). When we apply the transverse electric field (modeled by a zigzag potential), a positive field also points along z direction, from graphene to CGT (see also Fig. 1 in the main text).

The averaged calculated magnetic moments for all atom types and all twist angles are also summarized in Table S1. The magnetic moments of CGT are directly proportional to its lattice constant, as we find. In addition, the magnetic moments of the C atoms already give us a first hint that graphene experiences some proximity-induced magnetism from the CGT layer. For all twist angles, the C atoms have a small magnetic moment parallel to the Te atoms, but antiparallel to Cr and Ge atoms. However, we do not notice an obvious correspondence between the induced magnetism in graphene and the CGT magnetic moments. Here, the atomic registry should play a major role, i. e., even though the layers are twisted with respect to each other, at the moment we consider only a specific stacking configuration, with a certain amount of strain applied to the monolayers.

II. BAND STRUCTURE AND FIT RESULTS

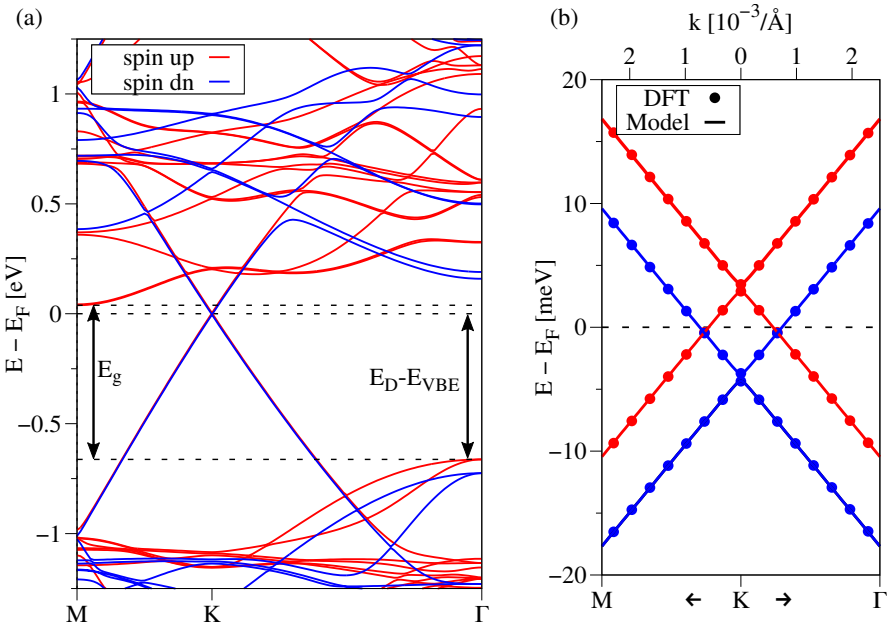

FIG. S2. (a) DFT-calculated band structure of the graphene/CGT heterostructure along the high-symmetry path M-K-Γ for a twist angle of 30°. Red (blue) solid lines correspond to spin up (spin down). We also define the CGT band gap, E_g, and the position of the Dirac point with respect to the valence band edge of CGT at the Γ point, $E_D - E_{VBE}$. (b) Zoom to the DFT-calculated (symbols) low energy Dirac bands near the K point with a fit to the model Hamiltonian (solid lines).

TABLE S2. Fit parameters of Hamiltonian $\mathcal{H}$ for the graphene/CGT heterostructures for different twist angles. We summarize the Fermi velocity v_F, the staggered potential Δ, proximity exchange parameters λ_{ex}^A and λ_{ex}^B, the Dirac point energy with respect to the Fermi level E_D, the band gap of CGT E_g, and the position of the Dirac point with respect to the valence band edge of CGT at the Γ point $E_D - E_{VBE}$.

twist angle [°]	v_F [10^5 m/s]	Δ [meV]	λ_{ex}^A [meV]	λ_{ex}^B [meV]	E_D [meV]	E_g [eV]	$E_D - E_{VBE}$ [eV]
0.0000	7.8555	0.000	4.201	4.199	-71.904	0.300	-0.080
3.0045	7.9972	0.054	4.079	4.116	-0.323	0.483	0.203
5.8175	8.0349	1.584	2.402	2.297	-0.520	0.629	0.554
8.9483	8.1209	0.048	1.181	1.133	-0.191	0.519	0.299
12.2163	7.9355	0.062	0.089	0.104	-0.054	0.474	0.129
14.7047	8.1996	0.172	-3.146	-3.167	-0.029	0.632	0.513
19.1066	7.8378	5.450	-2.050	1.331	-143.350	0.197	-0.168
23.4132	8.2224	0.128	-4.289	-4.200	1.669	0.717	0.716
26.9955	7.9568	0.149	-4.084	-3.957	0.349	0.460	0.095
30.0000	8.2856	0.298	-3.630	-3.596	-0.428	0.705	0.662

In Fig. S2, we show the results for the graphene/CGT heterostructure for a twist angle of 30°, corresponding to the supercell shown in Fig. S1. In agreement with recent calculations [12, 13], we find the Dirac cone located at the Fermi level and close to the conduction band edge of the CGT at the M point. The band gap of the CGT is about 0.7 eV and indirect (Γ → M), consistent with the tensile-strained lattice constant in the 30° case and the strain-tunable band gap of CGT [19, 20]. However, for different twist angles the situation can be rather different. Of importance for us is the location of the Dirac point with respect to the Fermi level, i. e., the doping of graphene, that we measure with the parameter E_D. Another important quantity is the band gap of the CGT, E_g, which is related to strain. Finally we extract the position of the Dirac point within the CGT band gap, by measuring the energy difference to the CGT valence band edge at the Γ point, i. e., $E_D - E_{VBE}$, as defined in Fig. S2(a). All those quantities are summarized in Table S2 for the different twist angles.

In Fig. S2(b), we show a zoom to the Dirac point of graphene with a fit to the model Hamiltonian from the main text. The results are in perfect agreement, employing the parameters in Table S2. For the 30° case, we find that

the spin down (spin up) Dirac cone is shifted towards lower (higher) energies. Here, proximity-induced exchange is similar to the Zeeman splitting from an external magnetic field [21]. The corresponding sublattice-dependent exchange parameters have the same sign and are nearly equal in value, $\lambda_{\rm ex}^{\rm A} \approx \lambda_{\rm ex}^{\rm B} \approx -3.6$ meV, hence we speak of uniform (ferromagnetic) proximity exchange.

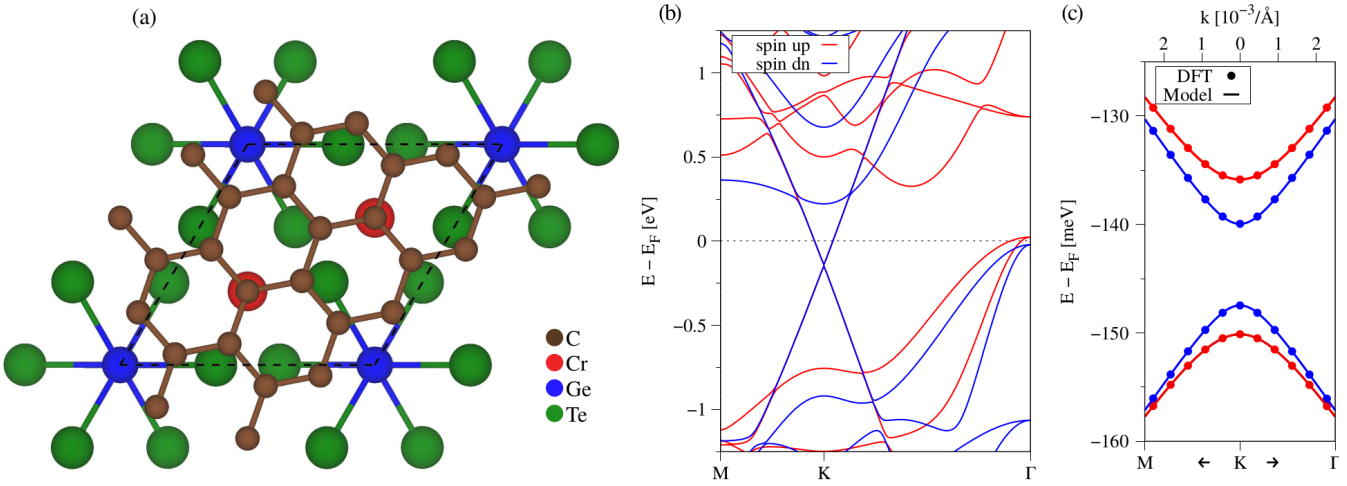

FIG. S3. (a) Bottom view of the graphene/CGT heterostructure with a twist angle of 19.1°. (b) DFT-calculated band structure along the high-symmetry path M-K-Γ. Red (blue) solid lines correspond to spin up (spin down). (c) Zoom to the DFT-calculated (symbols) low energy Dirac bands near the K point with a fit to the model Hamiltonian (solid lines).

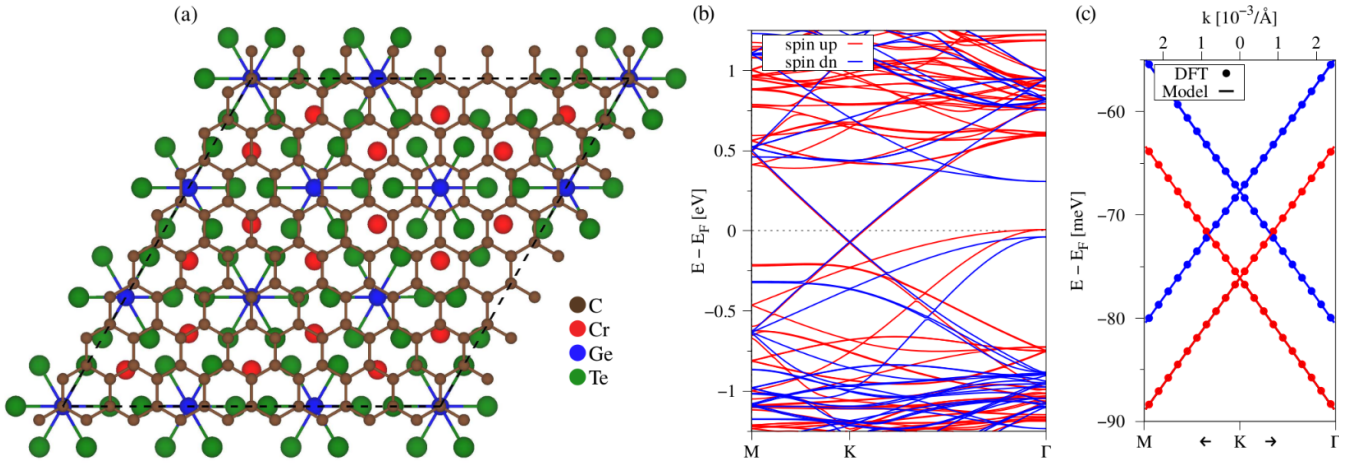

FIG. S4. (a) Bottom view of the graphene/CGT heterostructure with a twist angle of 0°. (b) DFT-calculated band structure along the high-symmetry path M-K-Γ. Red (blue) solid lines correspond to spin up (spin down). (c) Zoom to the DFT-calculated (symbols) low energy Dirac bands near the K point with a fit to the model Hamiltonian (solid lines).

Comparing the different twist angles, see Table S2, we find a nearly continuous tunability of proximity exchange parameters from about 4 to −4 meV, when twisting from 0° to 30°. In addition, we find some very surprising results. For 30°, we have uniform proximity exchange as already mentioned. Similarly, for 0° we also have uniform proximity exchange (4.2 meV), but the parameters have the opposite sign compared to the 30° case (−3.6 meV). Even more surprising, at an angle of 19.1° we find $\lambda_{\rm ex}^{\rm A} < 0$ and $\lambda_{\rm ex}^{\rm B} > 0$, i. e., staggered (antiferromagnetic) proximity-induced exchange, which is highly important for the realization of topological edge states in graphene [22]. Moreover, in some cases graphene experiences significant doping effects (0° and 19.1°) since $E_{\rm D}$ is below the Fermi level and also below the CGT valence band edge. In Fig. S3 and Fig. S4, we show the geometries, the calculated band structures, and fit results for the 19.1° and 0° cases, also perfectly matching with the model.

III. THE INFLUENCE OF STRAIN

TABLE S3. Structural information for the graphene/CGT heterostructures, when the CGT lattice constant is fixed at roughly 6.85 Å. We list the twist angle between the layers, the lattice constants of graphene and CGT, the calculated dipole of the structure, and the relaxed interlayer distance d_{int}.

twist angle [°]	a_{grp} [Å]	a_{CGT} [Å]	dipole [debye]	d_{int} [Å]
0.0000	2.5679	6.8475	-2.7303	3.6005
3.0045	2.4873	6.8506	-4.4405	3.5382
5.8175	2.4050	6.8480	-3.6099	3.5300
8.9483	2.4600	6.8480	-1.5072	3.5473
12.2163	2.5105	6.8500	-3.1492	3.5688
14.7047	2.4086	6.8480	-5.0438	3.5180
19.1066	2.5873	6.8454	-0.2760	3.6187
23.4132	2.3537	6.8400	-4.4003	3.5028
26.9955	2.5125	6.8475	-2.5066	3.5713
30.0000	2.3702	6.8423	-1.4053	3.4940

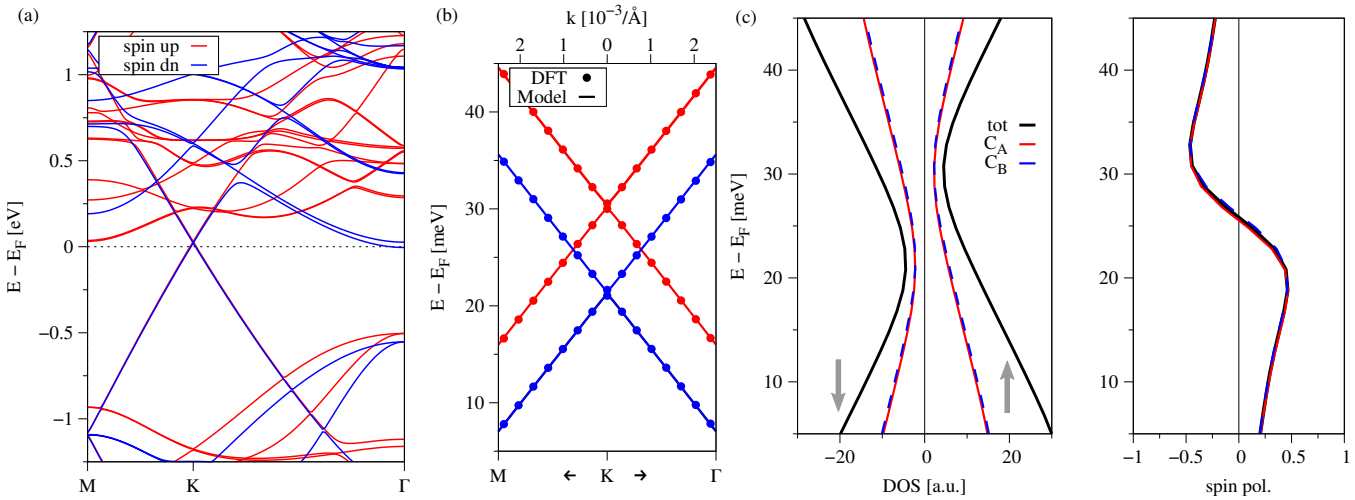

FIG. S5. (a) DFT-calculated band structure of the graphene/CGT heterostructure along the high-symmetry path M-K-Γ for a twist angle of 30° and when the CGT lattice constant is about 6.85 Å. Red (blue) solid lines correspond to spin up (spin down). (b) Zoom to the DFT-calculated (symbols) low energy Dirac bands near the K point with a fit to the model Hamiltonian (solid lines). (c) The sublattice (red = C_A, blue = C_B, black = total) and spin-resolved (positive = ↑, negative = ↓) density of states (DOS) of graphene near the Dirac point. The spin polarizations, calculated from the density of states as $(N_\uparrow - N_\downarrow)/(N_\uparrow + N_\downarrow)$.

So far, for each twist angle we distributed the strain to both materials (graphene and CGT) to form commensurate heterostructure supercells. Thus, we cannot a priori distinguish which results are due to straining, twisting, or a combination of both. Since the exchange coupling in graphene originates from CGT, we reconsider all structures with the different twist angles, but strain the heterostructure supercells such that the CGT lattice constant is always at about 6.85 Å, close to the experimental value. As a consequence, the strain applied to graphene increases, which should mainly influence the nearest neighbor hopping constant, reflected in the Fermi velocity. In Table S3, we again summarize the individual lattice constants of graphene and CGT for the different twist angles. Similar to before, we again allow the CGT atoms to relax their positions, while keeping the graphene layer fixed. Therefore, the interlayer distance may change, while the rippling of graphene stays fixed. Comparing Table S1 and Table S3, we can see that the interlayer distances change by at maximum 2%, which will certainly influence the magnitude, but not the type (uniform or staggered) of proximity-induced exchange coupling [12, 22]. In addition, the dipole (internal electric field) of the structure is slightly influenced, which will have an impact on the relevant band offsets.

In the same manner as above, we calculate the electronic band structure and apply our model Hamiltonian to the proximitized low energy Dirac bands. In Fig. S5, we again show the band structure of the graphene/CGT heterostructure for a twist angle of 30°, but now with a CGT lattice constant of about 6.85 Å. The overall band structure features remain the same, but the CGT now has a direct band gap at the Γ point, while the Dirac point is

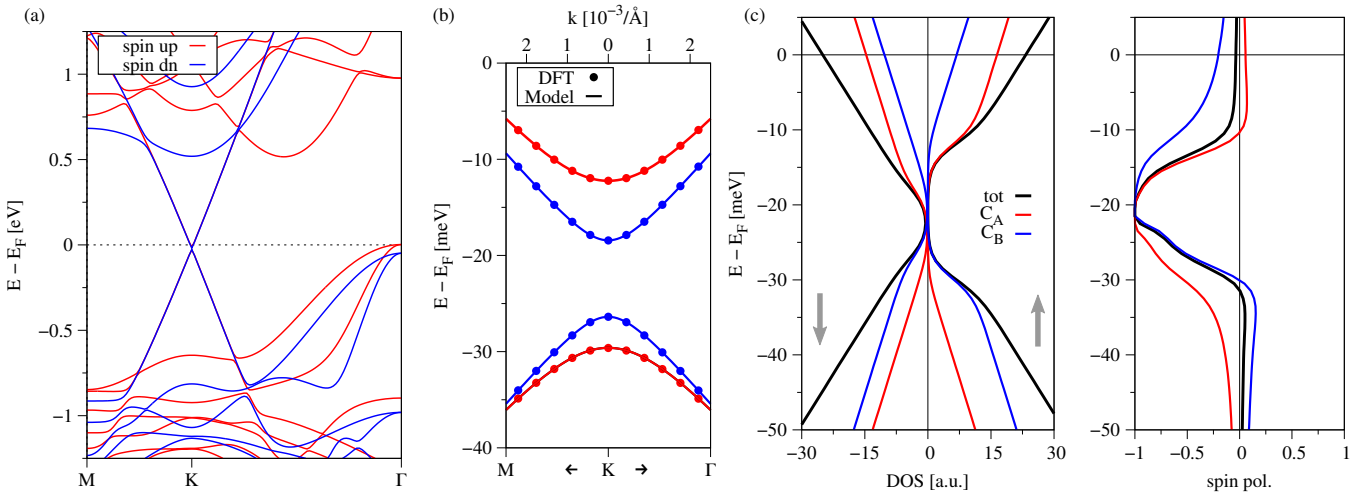

FIG. S6. (a) DFT-calculated band structure of the graphene/CGT heterostructure along the high-symmetry path M-K-Γ for a twist angle of 19.1° and when the CGT lattice constant is about 6.85 Å. Red (blue) solid lines correspond to spin up (spin down). (b) Zoom to the DFT-calculated (symbols) low energy Dirac bands near the K point with a fit to the model Hamiltonian (solid lines). (c) The sublattice (red = C_A, blue = C_B, black = total) and spin-resolved (positive = ↑, negative = ↓) density of states (DOS) of graphene near the Dirac point. The spin polarizations, calculated from the density of states as $(N_\uparrow - N_\downarrow)/(N_\uparrow + N_\downarrow)$.

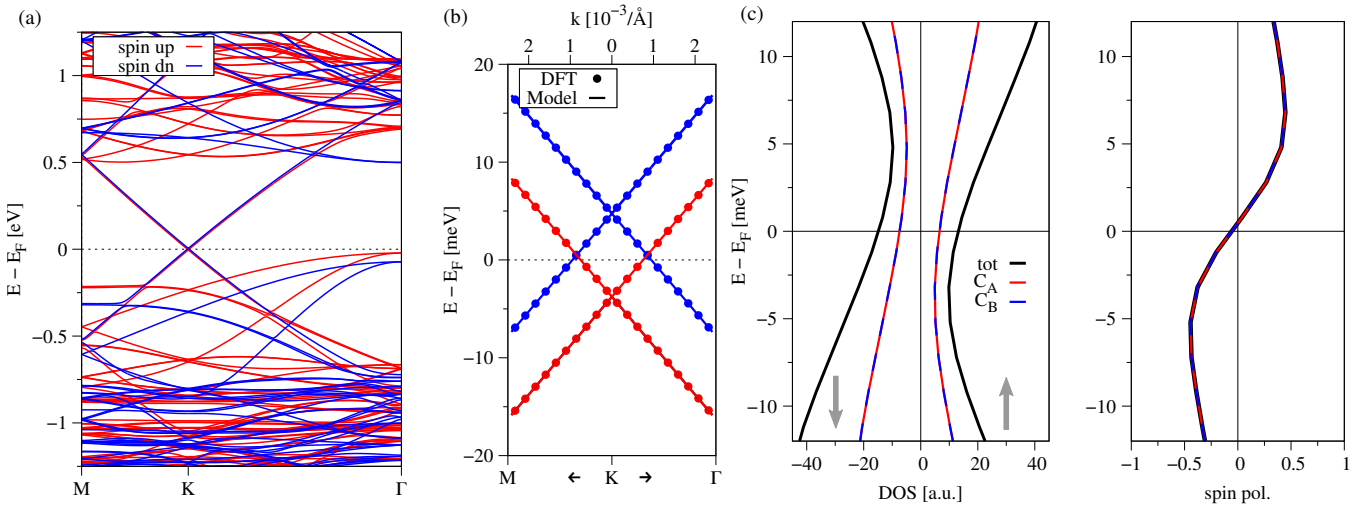

FIG. S7. (a) DFT-calculated band structure of the graphene/CGT heterostructure along the high-symmetry path M-K-Γ for a twist angle of 0° and when the CGT lattice constant is about 6.85 Å. Red (blue) solid lines correspond to spin up (spin down). (b) Zoom to the DFT-calculated (symbols) low energy Dirac bands near the K point with a fit to the model Hamiltonian (solid lines). (c) The sublattice (red = C_A, blue = C_B, black = total) and spin-resolved (positive = ↑, negative = ↓) density of states (DOS) of graphene near the Dirac point. The spin polarizations, calculated from the density of states as $(N_\uparrow - N_\downarrow)/(N_\uparrow + N_\downarrow)$.

located about 25 meV above the Fermi level. The calculated spin- and sublattice-resolved density of states together with the corresponding spin polarization of the Dirac states is shown in Fig. S5 (c). At about 40 meV above the Fermi level, the C_A (C_B) sublattice contributes with 51% (49%) and at 10 meV the contributions are switched, which is consistent with the tiny sublattice symmetry breaking Δ for the 30° structure. Above (below) the Dirac point, both sublattice spin polarizations are almost equal and negative (positive). The most important quantity for Hanle spin relaxation experiments [23] is the total spin polarization on graphene, which switches sign at the Dirac point, since the two spin densities become equal. At 40 meV (10 meV), the total spin polarization equals −29% (26%).

In Table S4, we summarize the same information as in Table S2, but for the heterostructures when CGT is nearly unstrained. First of all, we notice that the CGT band gap, E_g, stays nearly constant, due to almost similar CGT lattice constants for all twist angles. Moreover, the averaged magnetic moments of Cr, Ge, and Te atoms are 3.145, 0.025, and −0.089 μ_B and are nearly constant now. Thus, in Table S4, we list only the calculated magnetic moments

TABLE S4. Fit parameters of Hamiltonian $\mathcal{H}$ for the graphene/CGT heterostructures for different twist angles when the CGT lattice constant is fixed at roughly 6.85 Å. Parameters have the same meaning as in Table S2. We also list the averaged calculated magnetic moment of C atoms.

twist angle [°]	v_F [10^5 m/s]	Δ [meV]	λ_{ex}^A [meV]	λ_{ex}^B [meV]	E_D [meV]	E_g [eV]	$E_D - E_{VBE}$ [eV]	C [$10^{-3}\mu_B$]
0.0000	7.6032	0.002	4.252	4.249	0.488	0.522	0.022	-0.184
3.0045	7.9587	0.055	4.045	4.079	-0.265	0.522	0.224	-0.136
5.8175	8.2500	1.666	2.768	2.608	-0.358	0.522	0.478	-0.126
8.9483	8.1209	0.048	1.181	1.133	-0.191	0.519	0.299	-0.200
12.2163	7.8825	0.062	0.028	0.044	0.090	0.521	0.155	-0.221
14.7047	8.3861	0.217	-3.617	-3.630	-0.031	0.528	0.439	-0.271
19.1066	7.5375	6.329	-3.092	1.613	-21.664	0.514	-0.025	-0.243
23.4132	8.9630	0.145	-5.819	-5.560	55.749	0.516	0.576	-0.126
26.9955	7.8970	0.146	-3.878	-3.753	0.449	0.515	0.126	-0.242
30.0000	8.6758	0.288	-4.510	-4.427	25.804	0.500	0.530	-0.166

of C atoms. Second, the type and magnitude of proximity-induced exchange coupling stays nearly the same, i. e., straining does not dictate the proximity exchange, but the twisting does. Third, the Fermi velocity adapts itself to the new graphene lattice constant. Finally, the band offsets are drastically different for certain twist angles. For example, comparing the 0° results, we now find the Dirac point at the Fermi level and about 20 meV above the CGT valence band edge, see Table S4. In contrast, before we had the Dirac point at about −70 meV below the Fermi level and −80 meV below the CGT valence band edge, see Table S2. Similar scenarios hold for the other twist angles, but sometimes not as drastic as for the 0° case.

In Fig. S6 and Fig. S7, we show the band structure and density of states results for the 19.1° and 0° cases, when CGT is unstrained. For 19.1°, the conduction (valence) band Dirac states are mainly formed by C_A (C_B) p_z orbitals, which supports our sublattice resolved proximity exchange Hamiltonian with broken sublattice symmetry for arbitrary twist angles. At (−45 meV below) the Fermi level, the C_A atom contribution to the total graphene DOS is 65% (37%), while the C_B atom contribution is 35% (63%), see Fig. S6(c). At the Fermi level, the total spin polarization is negative (−3.6%), consistent with the conduction band Dirac dispersion. Nevertheless, the individual sublattice spin polarizations are opposite, positive for C_A and negative for C_B, supporting the antiferromagnetic proximity exchange that we have found by fitting the dispersion. For the valence band Dirac states, similar things hold, but spin polarizations and sublattice characters are reversed, compared to the conduction band states. At −45 meV below the Fermi level, the total spin polarization is 3.1%.

For 0°, see Fig. S7, we find similar results as for 30°, but the ferromagnetic proximity exchange has the opposite sign. Since the sublattice symmetry breaking Δ is nearly zero Dirac bands are equally formed by C_A and C_B sublattices. At about 10 meV (−10 meV) above (below) the Dirac point, the total spin polarization is positive (negative) and about 37% (−39%).

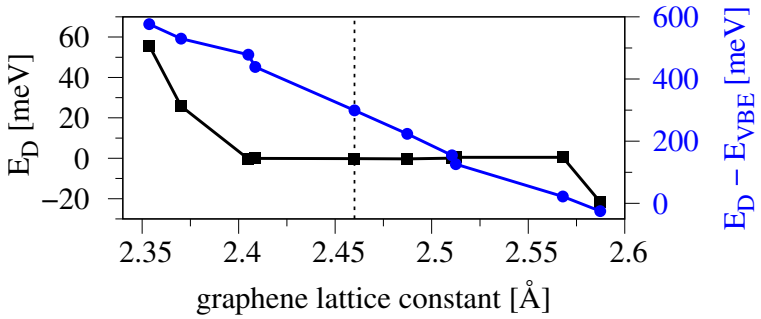

FIG. S8. The Dirac point energy E_D (black) and the band offset, $E_D - E_{VBE}$ (blue), as function of the graphene lattice constant. The information are listed in Tab. S3 and Tab. S4. The vertical dashed line indicates the experimental graphene lattice constant.

In Fig. S8, we plot the Dirac point energy, E_D, and the band offset, $E_D - E_{VBE}$, as function of the graphene lattice constant, as listed in Table S3 and Table S4. Astonishingly, we find a linear relationship between the band offset and the graphene lattice constant, which tells us that the strain in graphene is responsible for the different band offsets. Most important, we can now read off the *intrinsic* band offset of the heterostructure, that can be expected in experiment for all twist angles. The Dirac point should be located at the Fermi level and about 300 meV above

the CGT valence band edge for unstrained layers. In addition, if the graphene Dirac point is shifted out of the CGT band gap, i. e., if $E_g < (E_D - E_{VBE}) < 0$, graphene gets doped ($E_D \neq 0$). In our scenario, straining is responsible for the doping, but experimentally a gate voltage can be employed to tune the Dirac point within the CGT band gap, certainly influencing the proximity-induced exchange.

IV. ELECTRIC FIELD TUNABILITY

We have found that the proximity exchange depends on the twist angle. In addition, strain controls the band offset, also influencing proximity exchange. We now consider the first heterostructure set corresponding to Table S1 (graphene and CGT strained) with different twist angles and apply a transverse electric field between ±1.5 V/nm. Can we tune the proximity-induced exchange coupling by gating?

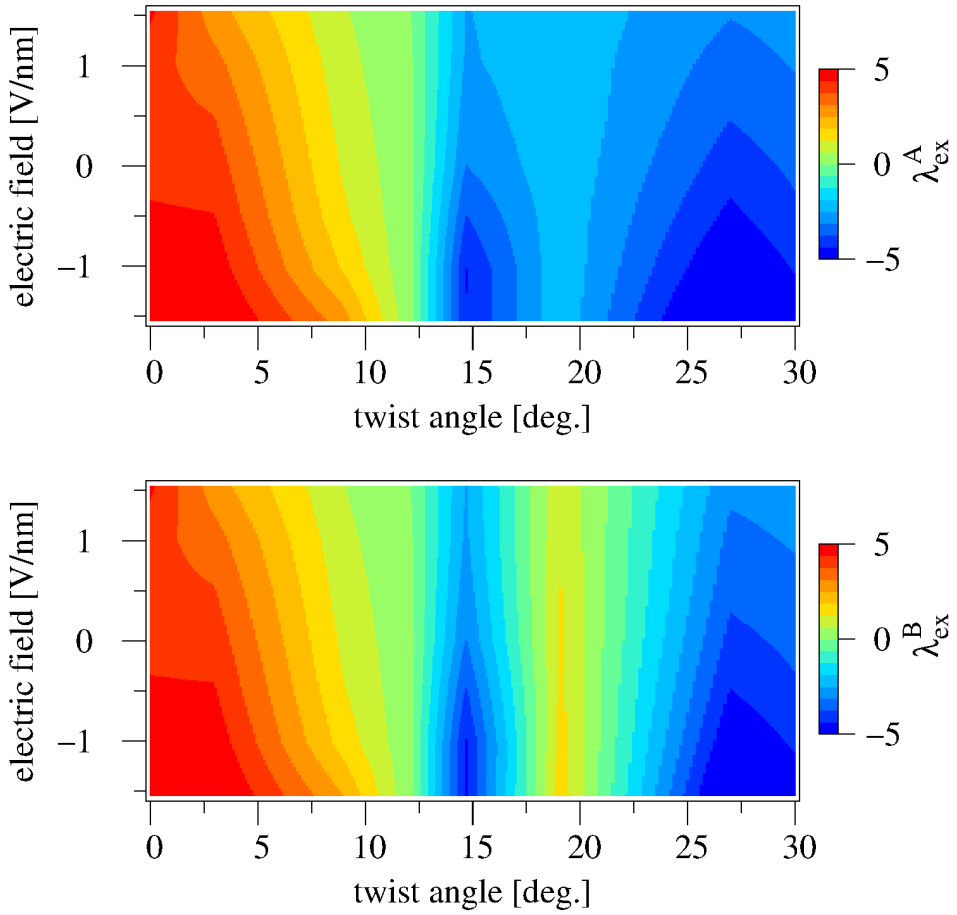

FIG. S9. Electric field and twist angle dependence of the two proximity-induced exchange parameters λ_{ex}^{A} (top) and λ_{ex}^{B} (bottom).

In Fig. S9, we summarize the electric field and twist angle dependence of the two proximity-induced exchange parameters λ_{ex}^{A} and λ_{ex}^{B}. In Table S5, we summarize the fit parameters employed for Fig. S9. We find that gating and twisting are two efficient control knobs to tailor the sign and magnitude of the proximity-induced exchange coupling in graphene/CGT heterostructures. In agreement with Table S2, one can nearly continuously tune the sign of the proximity exchange from positive to negative by twisting. In addition, an external electric field can be employed to tune the magnitude. For some twist angles, a relative tunability of more than 100% can be reached within our electric field limits. Most important, at a twist angle of 12.2°, proximity exchange parameters are small, but can be even tuned from positive to negative values by the gate field. Not only the proximity exchange can be tuned, but also the doping level, E_D, and the band offset, $E_D - E_{VBE}$, see Table S5. Unfortunately, our results always take into account the strain of the layers, which does not reflect the situation in experiments. Therefore, we can give at most predictions about the gate- and twist-tunability of the proximity exchange coupling. Note that for the electric field calculations, we have neglected two angles, 5.8° and 23.4°. The reason is that already small negative gate fields would shift the Dirac cone into the CGT conduction bands, leading to significant band hybridization and spoiling of the bare proximity exchange and the Dirac dispersion. However, the overall trends of the gate-tunable proximity exchange should still hold.

TABLE S5. Electric field dependence of the fit parameters of Hamiltonian $\mathcal{H}$ for the graphene/CGT heterostructures for different twist angles. We summarize the Fermi velocity v_F, the staggered potential Δ, proximity exchange parameters λ_{ex}^{A} and λ_{ex}^{B}, the Dirac point energy with respect to the Fermi level E_D, the position of the Dirac point with respect to the valence band edge of CGT at the Γ point $E_D - E_{VBE}$, and the calculated dipole of the structure.

el. field [V/nm]	twist angle [°]	v_F [10^5 m/s]	Δ [meV]	λ_{ex}^{A} [meV]	λ_{ex}^{B} [meV]	E_D [meV]	$E_D - E_{VBE}$ [eV]	dipole [debye]
-1.543	0.0000	7.8596	0.0006	5.2511	5.2508	-0.3157	0.0734	-14.7934
-1.028	0.0000	7.8606	0.0002	4.9167	4.9172	0.0422	0.0115	-10.8131
-0.514	0.0000	7.8596	0.0008	4.4663	4.4662	-13.0826	-0.0209	-6.5423
0.000	0.0000	7.8555	0.0001	4.2005	4.1994	-71.9042	-0.0798	-2.5453
0.514	0.0000	7.8477	0.0002	4.0489	4.0494	-131.5339	-0.1392	1.4452
1.028	0.0000	7.8274	0.0002	4.0131	4.0127	-192.3786	-0.2001	5.4117
1.543	0.0000	7.6683	0.0003	4.5233	4.5210	-199.8656	-0.2225	9.7786
-1.543	3.0045	8.0256	0.0589	5.1937	5.2226	0.4909	0.3815	-20.7561
-1.028	3.0045	8.0227	0.0567	4.7636	4.7939	-0.0705	0.3215	-15.3389
-0.514	3.0045	8.0135	0.0557	4.4071	4.4382	-0.2486	0.2621	-9.9093
0.000	3.0045	7.9972	0.0541	4.0791	4.1157	-0.3232	0.2026	-4.4864
0.514	3.0045	7.9713	0.0587	3.7419	3.7800	0.0305	0.1447	0.9421
1.028	3.0045	7.9302	0.0635	3.3389	3.3777	-0.1628	0.0868	6.3719
1.543	3.0045	7.8621	0.0687	2.7703	2.8025	0.0489	0.0300	11.8043
-1.543	8.9483	7.8864	0.1548	2.8482	2.5391	-0.0516	0.4841	-6.9494
-1.028	8.9483	8.0810	0.0877	1.8394	1.6477	0.5584	0.4235	-5.1303
-0.514	8.9483	8.1155	0.0607	1.4062	1.3342	-0.2144	0.3611	-3.3179
0.000	8.9483	8.1209	0.0475	1.1806	1.1331	-0.1914	0.2992	-1.5072
0.514	8.9483	8.1159	0.0416	1.0094	0.9692	0.3067	0.2369	0.3070
1.028	8.9483	8.1040	0.0370	0.8580	0.8160	-0.1417	0.1755	2.1149
1.543	8.9483	8.0855	0.0355	0.6986	0.6495	-0.0463	0.1137	3.9268
-1.543	12.2163	7.9494	0.0891	0.0484	0.0654	-0.0307	0.3165	-15.3657
-1.028	12.2163	7.9479	0.0784	0.0832	0.0965	0.6230	0.2548	-11.2889
-0.514	12.2163	7.9432	0.0704	0.0965	0.1067	-0.1465	0.1916	-7.2409
0.000	12.2163	7.9356	0.0619	0.0916	0.1005	-0.0538	0.1295	-3.1757
0.514	12.2163	7.9248	0.0565	0.0687	0.0723	-0.2459	0.0669	0.8752
1.028	12.2163	7.9110	0.0464	0.0275	0.0229	-0.0879	0.0064	4.9510
1.543	12.2163	7.9018	0.0442	-0.0192	-0.0248	-19.4284	-0.0276	9.2931
-1.543	14.7047	8.1085	0.2480	-4.3889	-4.4529	26.3551	0.6529	-22.3183
-1.028	14.7047	8.1398	0.2102	-4.4075	-4.4966	2.9413	0.6243	-16.2363
-0.514	14.7047	8.1745	0.1926	-3.7977	-3.8629	0.7328	0.5754	-10.4690
0.000	14.7047	8.1996	0.1727	-3.1462	-3.1669	-0.0287	0.5127	-4.9073
0.514	14.7047	8.2127	0.1428	-2.8358	-2.8646	-0.1019	0.4510	0.6701
1.028	14.7047	8.2189	0.1355	-2.5872	-2.6134	-0.0568	0.3890	6.2426
1.543	14.7047	8.2203	0.1355	-2.5296	-2.5499	0.4126	0.3274	11.8259
-1.543	19.1066	7.8418	5.3188	-2.0396	1.6232	-33.8931	-0.0392	-1.6063
-1.028	19.1066	7.8400	5.3783	-2.0338	1.5096	-97.2511	-0.0993	-1.1669
-0.514	19.1066	7.8384	5.4110	-2.0734	1.3874	-132.8669	-0.1461	-0.7137
0.000	19.1066	7.8378	5.4503	-2.0498	1.3314	-143.3497	-0.1680	-0.2338
0.514	19.1066	7.8350	5.5173	-2.0321	1.2987	-190.5737	-0.2169	0.2187
1.028	19.1066	7.8320	5.5899	-2.0911	1.1936	-230.1734	-0.2629	0.6699
1.543	19.1066	7.8307	5.6359	-2.0944	1.1650	-238.8009	-0.2867	1.1496
-1.543	26.9955	7.9018	0.1907	-5.9643	-5.7640	0.2573	0.2799	-12.0090
-1.028	26.9955	7.9275	0.1725	-5.1814	-5.0074	1.1925	0.2197	-8.8315
-0.514	26.9955	7.9450	0.1648	-4.5646	-4.4206	1.1464	0.1582	-5.6726
0.000	26.9955	7.9568	0.1496	-4.0845	-3.9566	0.3491	0.0952	-2.5319
0.514	26.9955	7.9643	0.1398	-3.7125	-3.5897	-0.2120	0.0323	0.6153
1.028	26.9955	7.9677	0.1345	-3.3923	-3.2929	-9.2685	-0.0143	3.8887
1.543	26.9955	7.9697	0.1342	-3.0823	-2.9970	-65.4473	-0.0710	7.0871
-1.543	30.0000	8.2439	0.3676	-4.8155	-4.7776	112.1088	0.8114	-5.7332
-1.028	30.0000	8.2572	0.3521	-4.3315	-4.2944	86.2641	0.7787	-4.1952
-0.514	30.0000	8.2745	0.3222	-3.8842	-3.8495	23.6695	0.7172	-2.7585
0.000	30.0000	8.2856	0.2983	-3.6302	-3.5964	-0.4279	0.6621	-1.3044
0.514	30.0000	8.2945	0.2756	-3.3269	-3.2935	-0.3483	0.6001	0.1250
1.028	30.0000	8.3005	0.2603	-3.0822	-3.0535	-0.1490	0.5377	1.5561
1.543	30.0000	8.3045	0.2488	-2.8847	-2.8606	0.3343	0.4766	2.9846

V. LATERALLY AND VERTICALLY SHIFTING THE LAYERS

How sensitive is the proximity-induced exchange coupling with respect to the atomic registry and the interlayer distance? For this purpose, we consider only the most important twist angles, i. e., 0°, 19.1°, and 30°, in order to cover all types of proximity exchange (uniform and staggered) and shift the graphene layer with respect to the CGT substrate. Again, we consider only the heterostructures where both layers are strained. We start from the relaxed structures as summarized in Table S1 and apply vertical shifts (z direction) of graphene, i. e., we tune the interlayer distance by Δd. For the lateral shifts (x and y), we use crystal coordinate notation, i. e., we shift graphene by fractions x and y of the supercell lattice vectors. In Table S6 we summarize the fit results.

TABLE S6. Fit parameters of Hamiltonian $\mathcal{H}$ for the graphene/CGT heterostructures for selected twist angles and for lateral (x and y) and vertical (z) shifts. The vertical shifts tune the interlayer distance by Δd, while lateral shifts x and y are in fractions of the supercell lattice vectors. Other parameters have the same meaning as in Table S2. We also list the averaged calculated magnetic moment of C atoms.

twist angle [°]	(x, y)	Δd [Å]	v_F [10^5 m/s]	Δ [meV]	λ_{ex}^A [meV]	λ_{ex}^B [meV]	E_D [meV]	$E_D - E_{VBE}$ [eV]	C [$10^{-3}\mu_B$]
0.0000	(0,0)	-0.1	7.7801	0.000	5.752	5.751	-119.931	-0.127	-0.308
0.0000	(0,0)	0.1	7.9063	0.002	3.066	3.064	-22.279	-0.031	-0.194
0.0000	(1/6,1/6)	0.0	7.8549	0.025	4.272	4.274	-71.123	-0.079	-0.249
0.0000	(1/9,2/9)	0.0	7.8537	0.117	4.280	4.253	-72.503	-0.080	-0.238
19.1066	(0,0)	-0.1	7.7793	7.862	-2.853	1.842	-192.029	-0.226	-0.264
19.1066	(0,0)	0.1	7.8764	3.794	-1.462	0.947	-134.069	-0.148	-0.157
19.1066	(2/3,1/3)	0.0	7.6762	3.924	-2.240	-4.033	-149.732	-0.177	-0.214
19.1066	(1/3,2/3)	0.0	7.6631	7.026	-2.407	-6.621	-148.355	-0.177	-0.193
30.0000	(0,0)	-0.1	8.2472	0.382	-4.593	-4.555	0.015	0.585	-0.248
30.0000	(0,0)	0.1	8.3140	0.233	-2.791	-2.761	33.910	0.724	-0.144
30.0000	(1/6,1/3)	0.0	8.2814	0.070	-3.578	-3.592	-0.149	0.662	-0.202
30.0000	(1/3,1/3)	0.0	8.2852	0.137	-3.607	-3.646	-0.131	0.663	-0.206

We find that the interlayer distance strongly influences the proximity exchange. Tuning Δd by ± 0.1 Å, which equals about $\pm 3\%$ of the interlayer distance only, the exchange parameters can be tuned by on average $\mp 30\%$. Such tunability has been recently reported for the proximity SOC in graphene/WSe_2 heterostructures, where a special experimental setup allows to apply hydrostatic pressure and tune the vdW gap between the layers [24, 25]. In addition, the interlayer distance also influences the doping and band offsets, as we can see from E_D and $E_D - E_{VBE}$. Increasing the distance, decreases the charge transfer between the layers and vice versa, also in agreement with experimental findings for graphene/MoS_2 heterostructures [26].

What about the lateral shifts? In the two cases, 0° and 30°, when the heterostructure supercell is large, the atomic registry does not play a role for the results, especially for proximity exchange couplings. The reason is, that on average the two C sublattices always feel rouhgly the same influence from the CGT layer, independent of the shift. However, for the 19.1° case, there is a strong dependence on the lateral shift, since the heterostructure supercell is small, see Fig. S3(a). Our original result of staggered exchange parameters, see Table S2, is not valid anymore when shifting the layers relative to each other, see Table S6. This makes the 19.1° case a special one, since we can achieve uniform and staggered exchange couplings, important for tailoring the edge transport properties in proximitized graphene [22].

VI. ENCAPSULATED STRUCTURES

Assume graphene to be encapsulated between two CGT layers. Depending on the twist angles (ϑ_b and ϑ_t) of bottom and top CGT layers with respect to graphene, and their individual magnetizatons ($\boldsymbol{M}_b$ and $\boldsymbol{M}_t$) we can further tailor proximity exchange coupling in graphene.

Case 1: When the magnetizations are parallel (antiparallel) and twist angles are the same, proximity exchange couplings are additive (effectively cancel) [12, 27].

Case 2: When the magnetizations are parallel and twist angles are different (say 0° and 30°), proximity exchange couplings can also vanish, based on the above results in Table S4.

Case 3: The magnetizations are parallel and both twist angles are 19.1°. Depending on the individual stacking configurations, one should be able to create a scenario of ferromagnetic (antiferromagnetic) proximity exchange from, say, bottom (top) CGT, based on Table S6. Consequently, the layer-dependent proximity exchange couplings could add up for one graphene sublattice, while for the other sublattice the couplings cancel each other.

In Fig. S10, we summarize the results for three exemplary structures of CGT encapsulated graphene, where both twist angles are 19.1° and parallel magnetizations, but with different encapsulation configurations. Similar to our non-encapsulated structures, we first performed a relaxation to obtain reasonable band structure results. Here, we also used structures where the CGT lattice constant is unstrained. Comparing the three cases, we find the global band structure to be barely different. However, the low energy graphene Dirac bands differ significantly. In the first case, the sublattice symmetry breaking Δ is large, opening a gap in the Dirac spectrum, and proximity exchange couplings are ferromagnetic. In the second case, Δ is also large, but proximity exchange couplings are antiferromagnetic. In the third case, we also find ferromagnetic couplings, but Δ is small leading to band overlap at the K point. For all three cases, proximity exchange parameters are also much larger than for the non-encapsulated structure. This demonstrates, that one can boost and further tailor proximity exchange in graphene by CGT encapsulation.

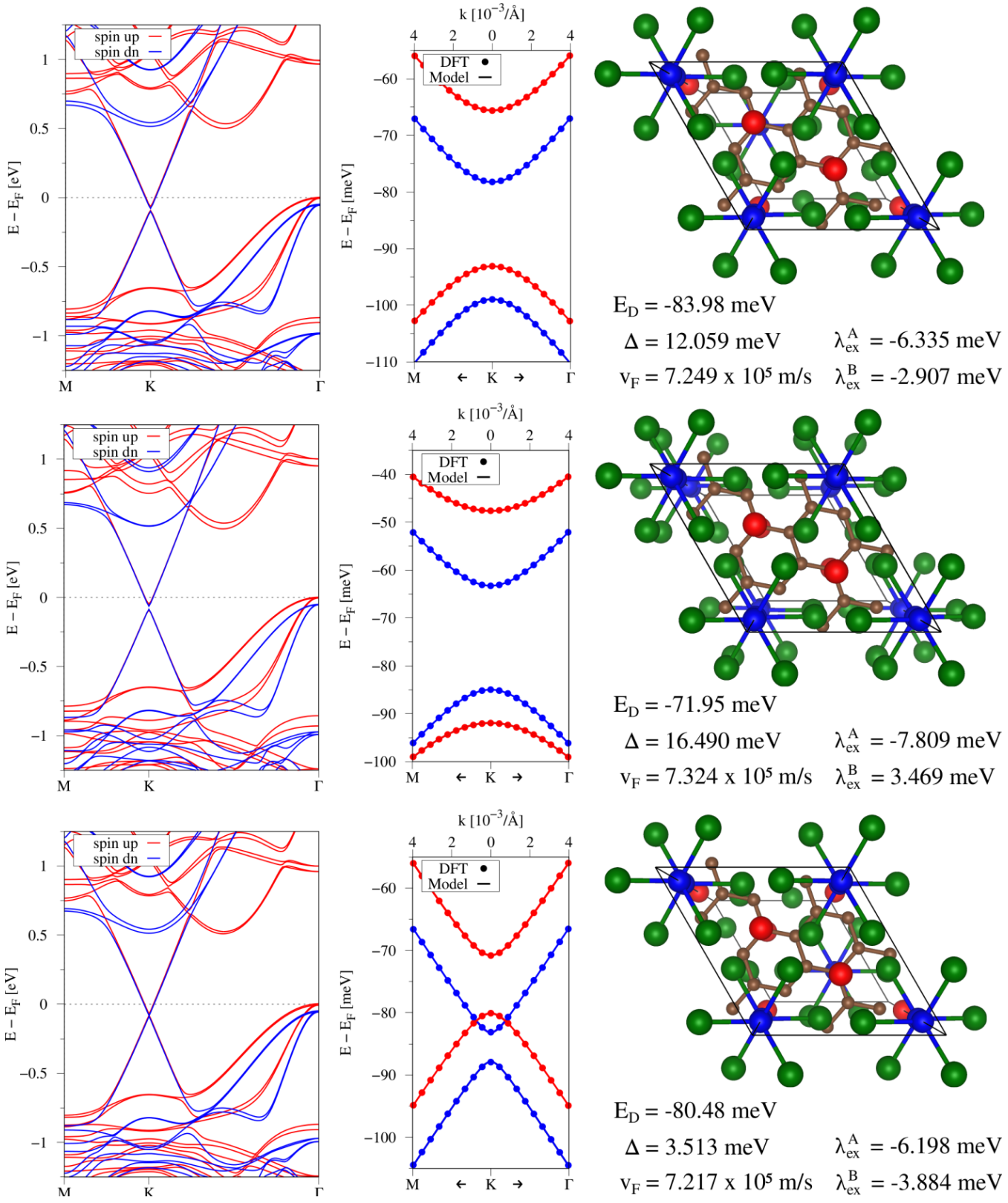

FIG. S10. Left: DFT-calculated band structures of the CGT/graphene/CGT heterostructures along the high-symmetry path M-K-Γ for twist angles of 19.1° and when the CGT lattice constant is about 6.85 Å. Red (blue) solid lines correspond to spin up (spin down). Middle: Zooms to the DFT-calculated (symbols) low energy Dirac bands near the K point with a fit to the model Hamiltonian (solid lines). Right: Top views of the corresponding geometries and fit parameters.

VII. ORIGIN OF PROXIMITY EXCHANGE

One of the main questions is: What causes the different proximity exchange couplings?

S1. Analyzing the local Density of States

We consider three important angles, 19.1° with antiferromagnetic proximity exchange, and 0° and 30° with opposite ferromagnetic proximity exchange. Here, we consider structures from Table S3 where CGT is unstrained. In Fig. S11, we again show the calculated dispersion, the spin and atom resolved local density of states (corresponding to the Dirac bands) and the spin polarization of Cr, Ge, and Te atoms. We have also calculated the spin polarizations in real space (Fig. S12, Fig. S13, and Fig. S14), $\Delta\rho = \rho_\uparrow - \rho_\downarrow$, where the spin densities $\rho_{\uparrow/\downarrow}(\boldsymbol{r}) = \sum_{n,\boldsymbol{k}} |\phi^{\boldsymbol{k}}_{n,\uparrow/\downarrow}(\boldsymbol{r})|^2$ are sums over eigenstates with the corresponding spin. To find out about the proximity exchange couplings, we take into account the Dirac states within the shaded regions in Fig. S11 for the calculation of spin densities (conduction and valence bands individually).

For 30°, we find an overall negative spin polarization on CGT that contributes to the Dirac spectrum, see Fig. S11. Looking at the decomposition of the DOS at about 40 meV above the Fermi level, the spin up (down) Dirac bands are formed by about 98.86% C, 0.35% Cr, 0.18% Ge, and 0.61% Te (97.27% C, 0.89% Cr, 0.82% Ge, and 1.02% Te). At about 10 meV above the Fermi level, the spin up (down) Dirac bands are formed by about 98.90% C, 0.33% Cr, 0.18% Ge, and 0.60% Te (97.43% C, 0.83% Cr, 0.78% Ge, and 0.96% Te). From Fig. S12, we find a negative (positive) spin polarization on graphene, when taking into account conduction (valence) band states only, consistent with the calculated density of states and the low energy bands, see Fig. S5. From Fig. S12 it is evident that there is mainly a coupling of graphene p_z orbitals to a spin down density on CGT (hence a significant negative spin polarization from CGT). From a simple perturbation theory point of view, coupling to a spin down density could lower the energy of spin down Dirac states, which is consistent with the Dirac spectrum for 30°.

For 0°, looking at the decomposition of the DOS at 10 meV above the Fermi level, the spin up (down) Dirac bands are formed by about 97.83% C, 0.66% Cr, 0.30% Ge, and 1.20% Te (98.03% C, 0.34% Cr, 0.38% Ge, and 1.25% Te). At about −10 meV below the Fermi level, we find that spin up (down) Dirac bands are formed by about 97.82% C, 0.66% Cr, 0.31% Ge, and 1.22% Te (97.95% C, 0.35% Cr, 0.39% Ge, and 1.31% Te). From this it is evident that there is mainly a coupling between graphene p_z to Te p orbitals. From the real space spin polarization, see Fig. S13, we find that conduction band Dirac states couple mainly to a positive spin density on Cr and non-interfacial Te atoms, while for the valence band there is a coupling to a negative spin density on interfacial Te atoms. Consistent with the DOS, see Fig. S7(c), we find positive (negative) spin polarization on graphene when considering conduction (valence) band Dirac states only. The spin polarizations are exactly opposite as for the 30° case.

For 19.1°, looking at the decomposition of the DOS at the Fermi level, the spin up (down) Dirac bands are formed by about 98.56% C, 0.21% Cr, 0.11% Ge, and 1.12% Te (98.98% C, 0.17% Cr, 0.12% Ge, and 0.73% Te). At about −45 meV below the Fermi level, we find that spin up (down) Dirac bands are formed by about 98.77% C, 0.28% Cr, 0.15% Ge, and 0.79% Te (99.00% C, 0.17% Cr, 0.16% Ge, and 0.67% Te). From Fig. S14, we observe opposite spin polarizations on the graphene sublattices, which supports our finding of antiferromagnetic exchange coupling. Consistent with the calculated density of states, see Fig. S6(c), we also see a change of the spin polarization on the graphene sublattices, when considering valence or conduction band states only.

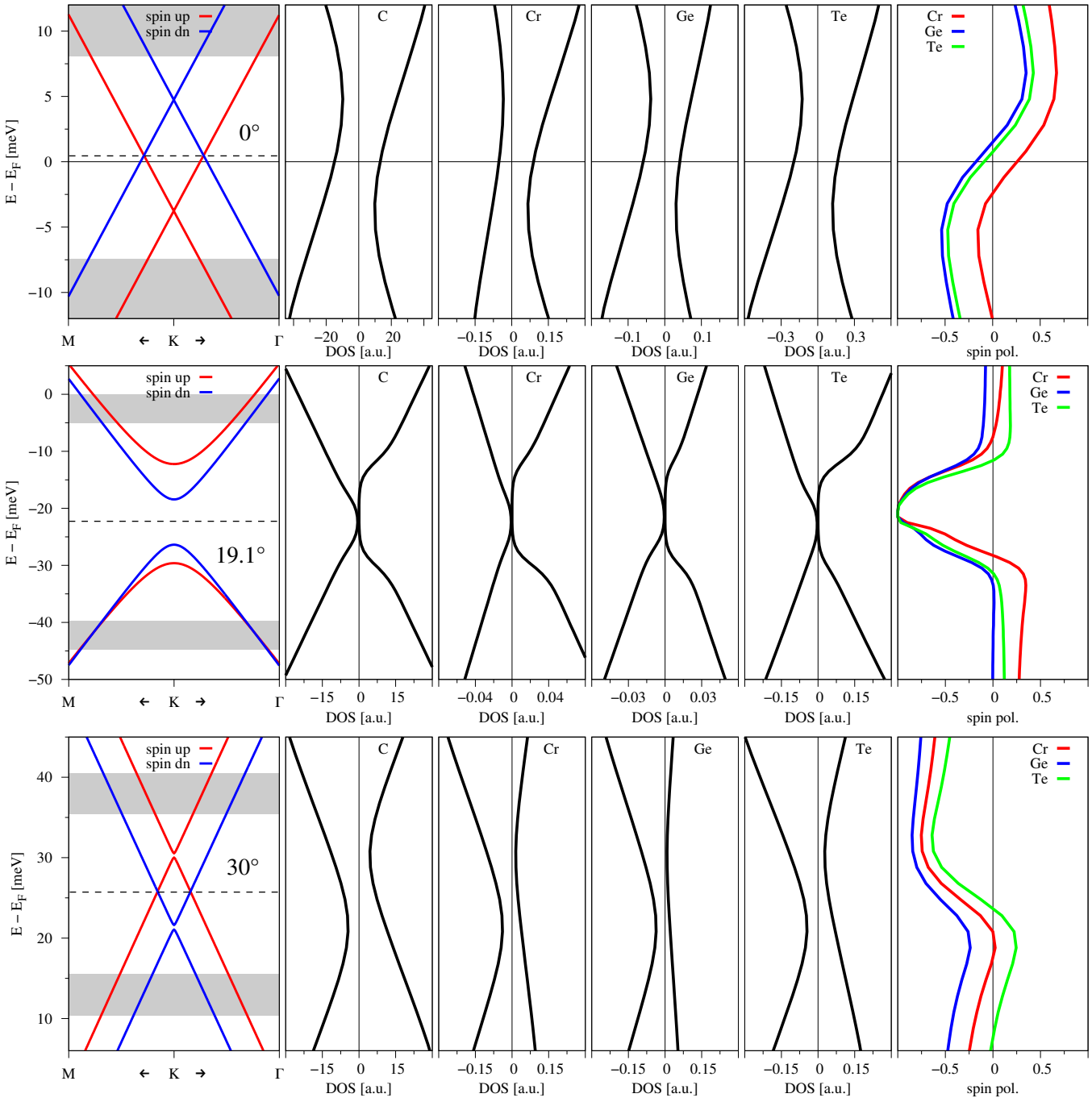

FIG. S11. For 0°, 19.1°, and 30°, we again show the low energy Dirac band structure. The dashed line indicates the Dirac point energy E_D. In addition, we show the corresponding atom and spin resolved local density of states, and the spin polarization calculated as $(N_\uparrow - N_\downarrow)/(N_\uparrow + N_\downarrow)$ for Cr, Ge, and Te atoms. The C density of states and spin polarization is investigated in more detail in Figs. S5, S6, and S7. The shaded regions are employed for the calculation of the spin densities in real space.

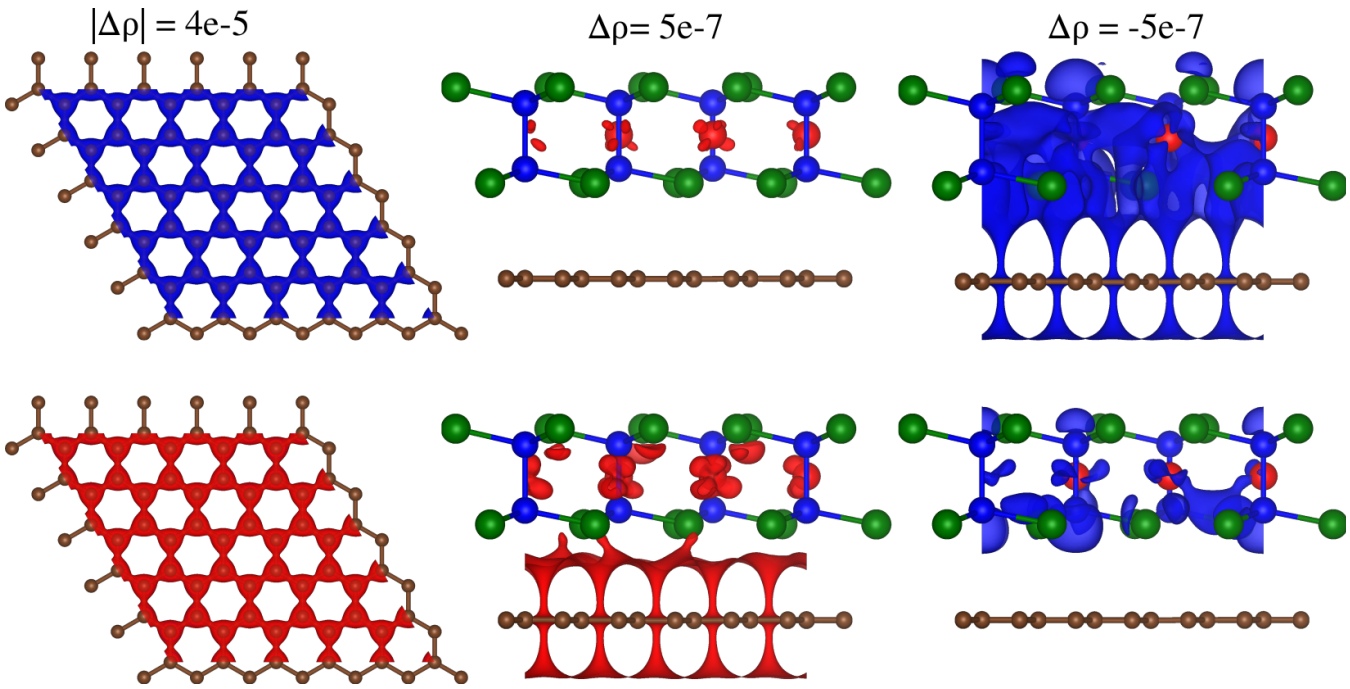

FIG. S12. Calculated spin polarization, $\Delta\rho = \rho_\uparrow - \rho_\downarrow$, for the graphene/CGT heterostructure with a twist angle of 30°. The color red (blue) corresponds to $\Delta\rho > 0$ ($\Delta\rho < 0$). The isosurfaces correspond to isovalues (units Å^{-3}) as indicated by the labels above the figures. Left: Top view on graphene only. Middle and Right: Side views of the full heterostructure. Upper (lower) row takes into account conduction band (valence band) states only.

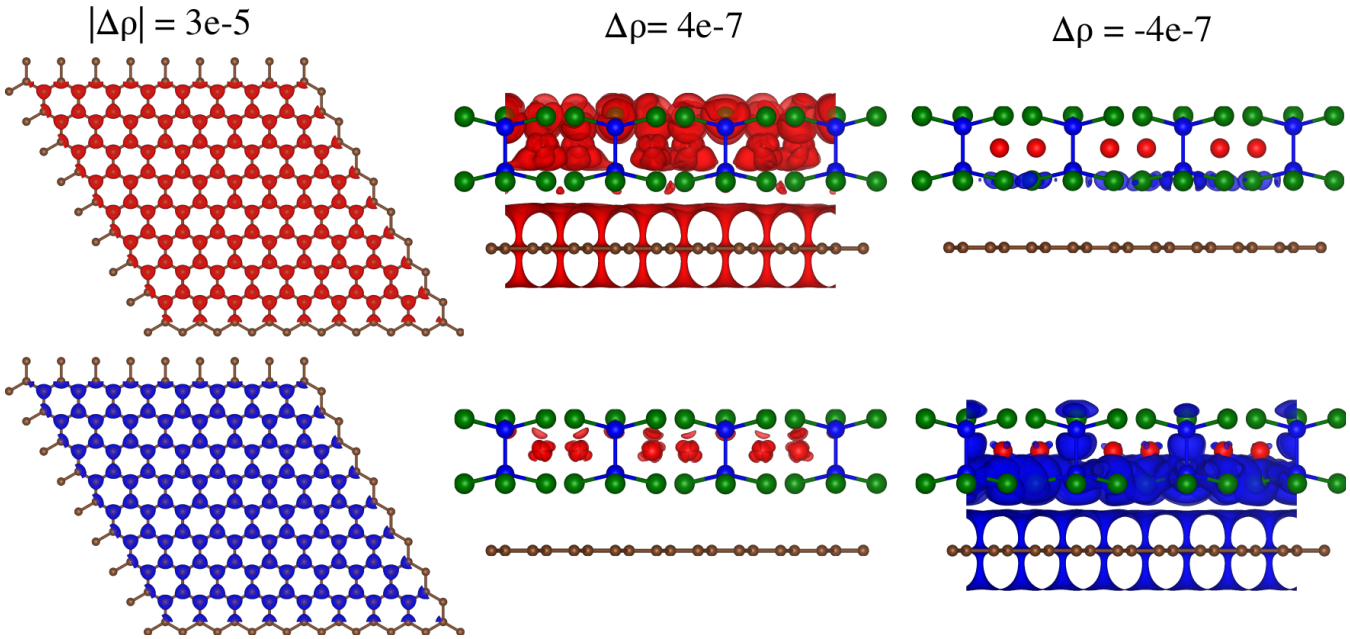

FIG. S13. Same as Fig. S12, but for a twist angle of 0°.

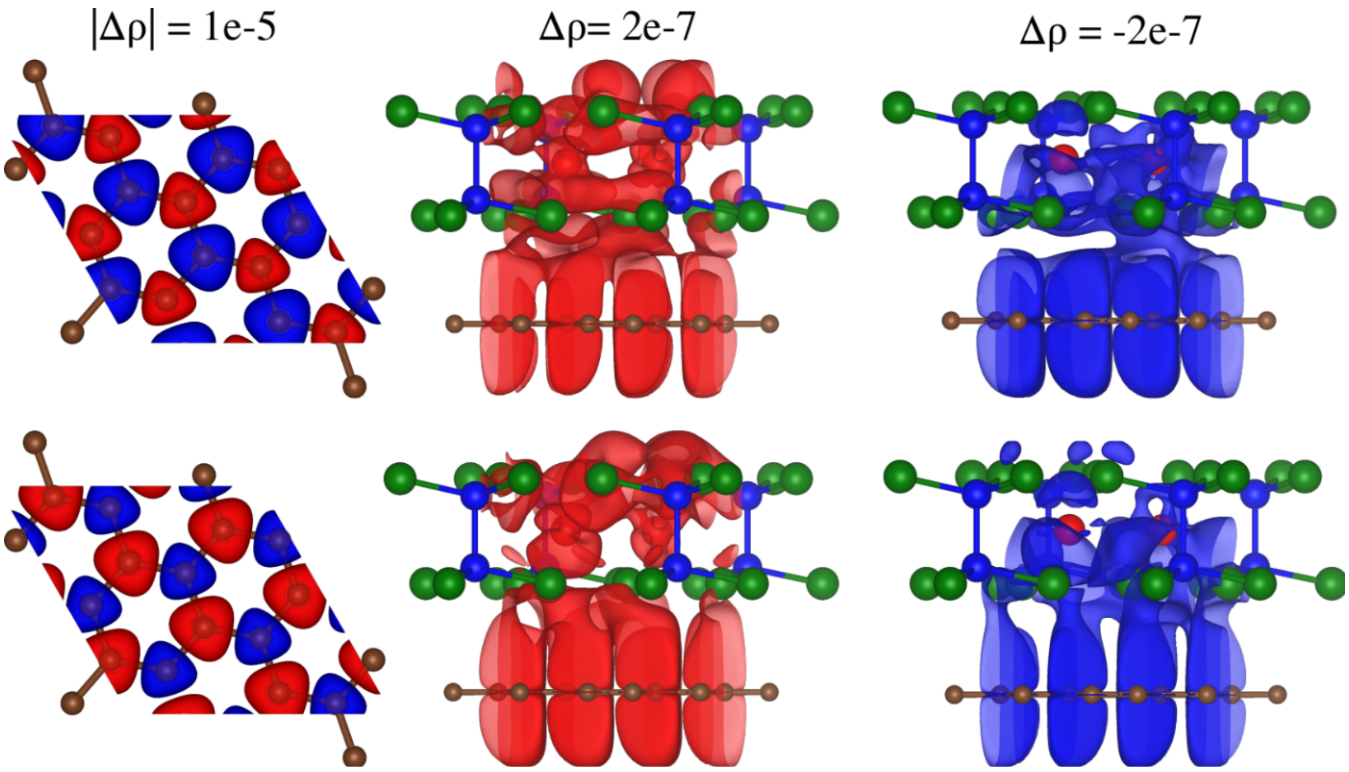

FIG. S14. Same as Fig. S12, but for a twist angle of 19.1°.

S2. Backfolding of the Dirac point

Recent tight-binding considerations of twisted graphene/TMDC heterostructures [28, 29] show that the Dirac states couple to different k points in the TMDC Brillouin zone for different twist angles, to ensure quasi momentum conservation. This can be potentially used to explain the different exchange couplings (and spin polarizations) we have found for our graphene/CGT heterostructures. In Fig. 5 in the main text we perform a similar analysis as in Refs. [28, 29]. Looking at the CGT monolayer band structure (Figs. S15, S16, and S17) and taking into account the backfolding of the graphene K point, as well as the band offsets for the different twist angles, we find that the Dirac states can couple to different bands of CGT.

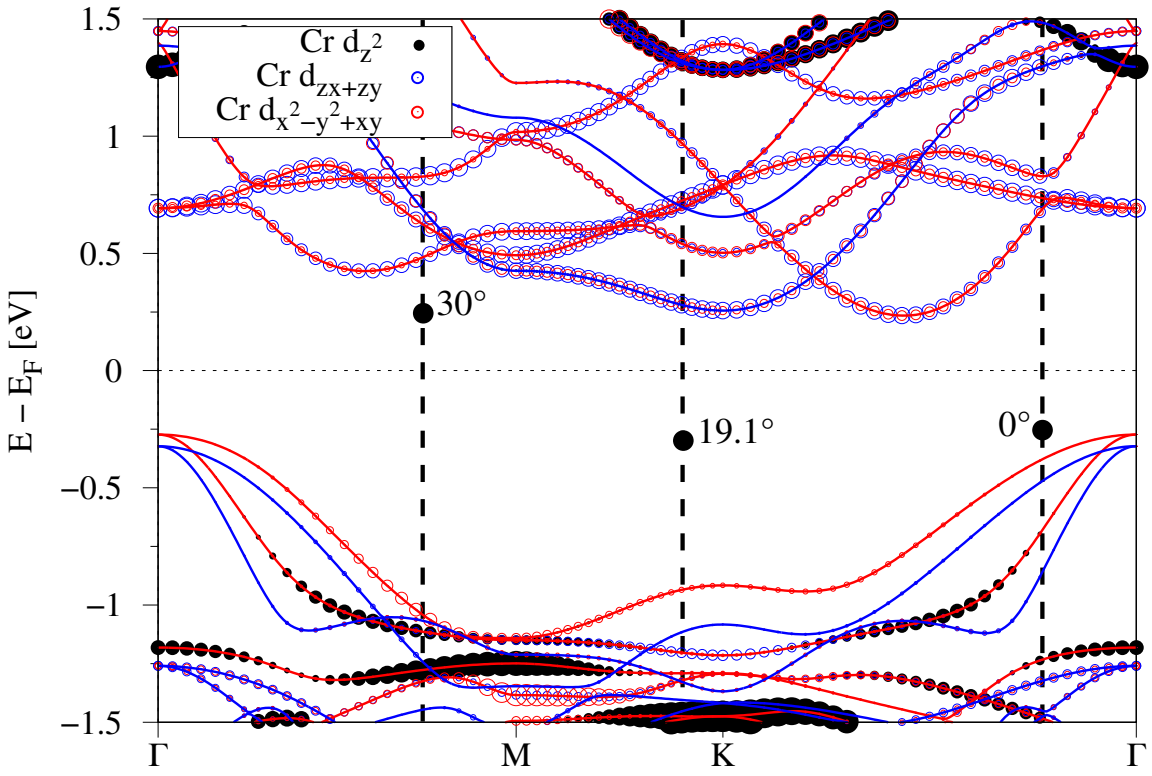

FIG. S15. DFT-calculated band structure of monolayer CGT, projected onto Cr d orbitals. The size of the symbols represent the contribution of the orbitals to a specific band and at a given k point. The color of the solid lines represent spin up (red) and spin down (blue). We also indicate the locations, to which the Dirac point backfolds, similar to Fig. 5.

From Fig. 5 it is evident that for 0°, the graphene Dirac states at the K point could predominantly couple to CGT valence band states near the Γ point. These CGT states are spin up and mainly formed by Te p orbitals, see Fig. S17. For 30° twist angle, we find the Dirac states very close to CGT conduction band states near the M point. These CGT bands are formed mainly by Cr d orbitals, see Fig. S15. For the 19.1° case, the Dirac states can couple to CGT bands near the K point. Here, the Dirac point is located nearly in the middle of CGT valence (formed by Te p orbitals) and conduction (formed by Cr d and Ge p orbitals) bands, so that coupling to both seems reasonable. The competition between the couplings could effectively lead to antiferromagnetic proximity exchange. Our analysis can at least give indications about the different proximity exchange. What certainly also matters, as we have seen especially for the 19.1° twist angle, is the precise atomic registry of graphene above CGT.

In addition, the band offset of the Dirac bands with respect to the TMDC band edges was found to be important [28, 29]. Also here, the location of the Dirac bands with respect to the CGT bands plays a major role for the proximity exchange coupling, as we have found from our electric field results. From Table S5, we find that the closer the Dirac point is to the CGT conduction band edge, the larger in magnitude are the proximity exchange parameters (except for 12.2°).

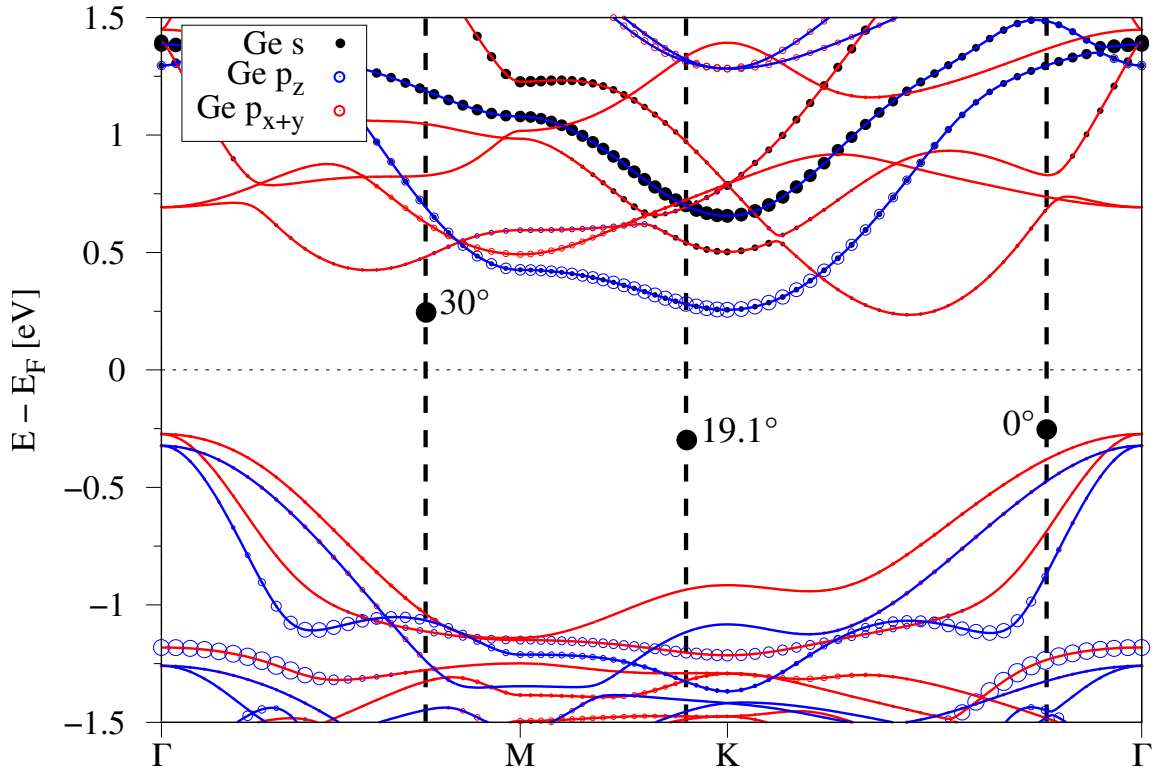

FIG. S16. Same as Fig. S15, but projected onto Ge s and p orbitals.

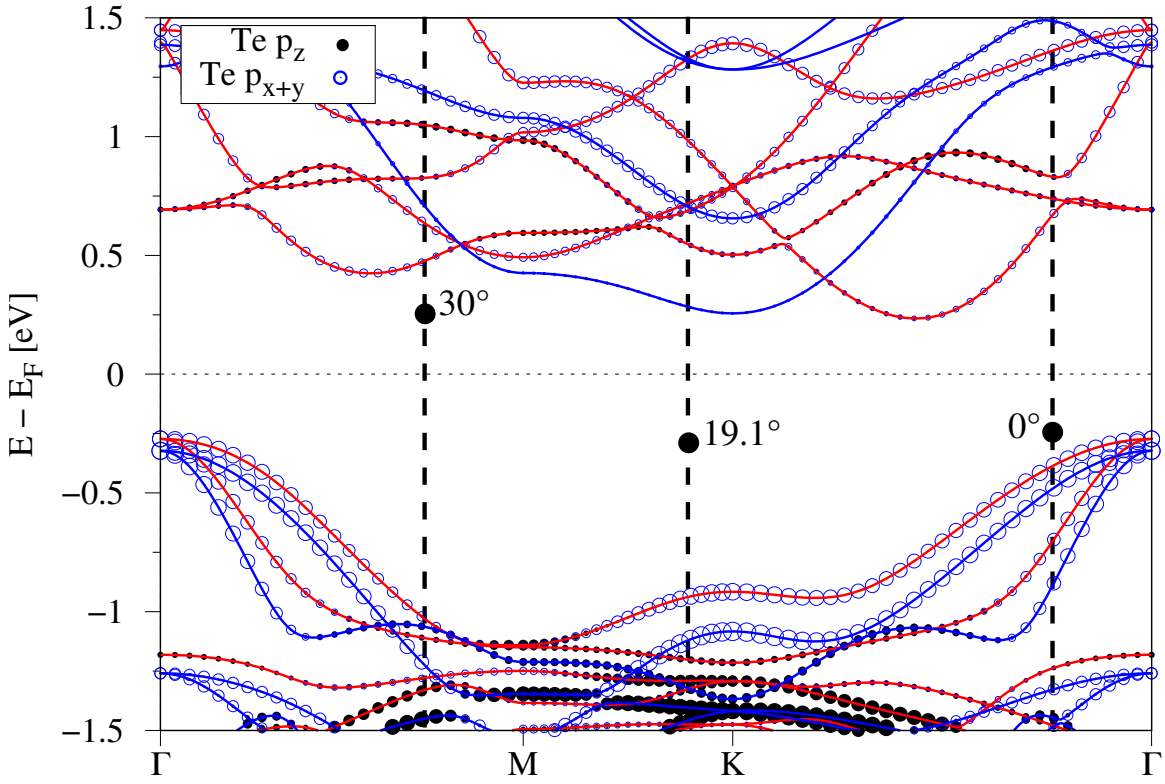

FIG. S17. Same as Fig. S15, but projected onto Te p orbitals.

S3. Anticrossings in projected band structure

Another helpful tool is to look for anticrossings between Dirac and CGT states in the projected band structure, see Fig. S18. We now believe, that this is most important to find out about the different proximity exchange couplings. For example, in the case of 30°, the Dirac states are very close to CGT spin up conduction bands, see Fig. S5(a). Also the backfolding picture would suggest a coupling to the energetically closest CGT spin up conduction bands, see Fig. 5. If such a coupling would be present, then spin up Dirac bands would be lowered in energy (considering simple perturbation theory), which is contrary to the low energy Dirac dispersion, see Fig. S5(b). From the projected band structure, we find that the coupling happens predominantly with CGT spin down conduction bands, as the pronounced anticrossings suggest [see the grey circles in Fig. S18]. The coupling to CGT spin down conduction bands lowers the spin down Dirac states in energy, consistent with the low energy dispersion for 30°. Such a band hybridization/anticrossing picture has been previously discussed in Ref. [30]. The coupling spin down states is also consistent with the local density of states and the spin polarization that we have found, see Fig. S11 and Fig. S12.

Let us do the same analysis for the other angles. In the case of 0°, the Dirac states are close to CGT spin up valence bands, see Fig. S7(a) and Fig. 5. This would lead to a raise of spin up Dirac bands in energy, which is again contrary to the calculated low energy dispersion, see Fig. S7(b). Looking at the projected band structure, the main anticrossing is between CGT spin up conduction bands with Dirac states. This coupling lowers the spin up Dirac bands in energy, consistent with the low energy dispersion for 0°. Again, this is also consistent with the local density of states and the spin polarization we have found, see Fig. S11 and Fig. S13, where a positive CGT spin polarization contributes to the conduction band Dirac states. In addition, a negative CGT spin polarization contributes to the valence band Dirac states, which leads to the same conclusion.

In the case of 19.1°, the first anticrossing in the conduction band is with CGT spin down bands, which lowers conduction band Dirac states in energy, consistent with the calculated low energy dispersion, see Fig. S6(b). For the valence band Dirac states, there are anticrossings with spin up and spin down CGT bands. In total, the interplay of all these couplings effectively leads to the observed antiferromagnetic proximity exchange in the low energy Dirac spectrum.

Finally, we would like to say a few words about the sensitivity of proximity exchange to the atomic registry in the case of 19.1°. In Fig. S19, we show the global band structures for two different lateral shifts, as listed in Table S6, where we also highlight band anticrossings. Without the shift ($x = 0, y = 0$) we get antiferromagnetic proximity exchange and barely anticrossings. For a different atomic registry ($x = 1/3, y = 2/3$), we get ferromagnetic proximity exchange and highly pronounced anticrossings. From that we can see that the atomic registry plays a highly important role for interlayer coupling and the proximity exchange. This is especially valid for small supercells.

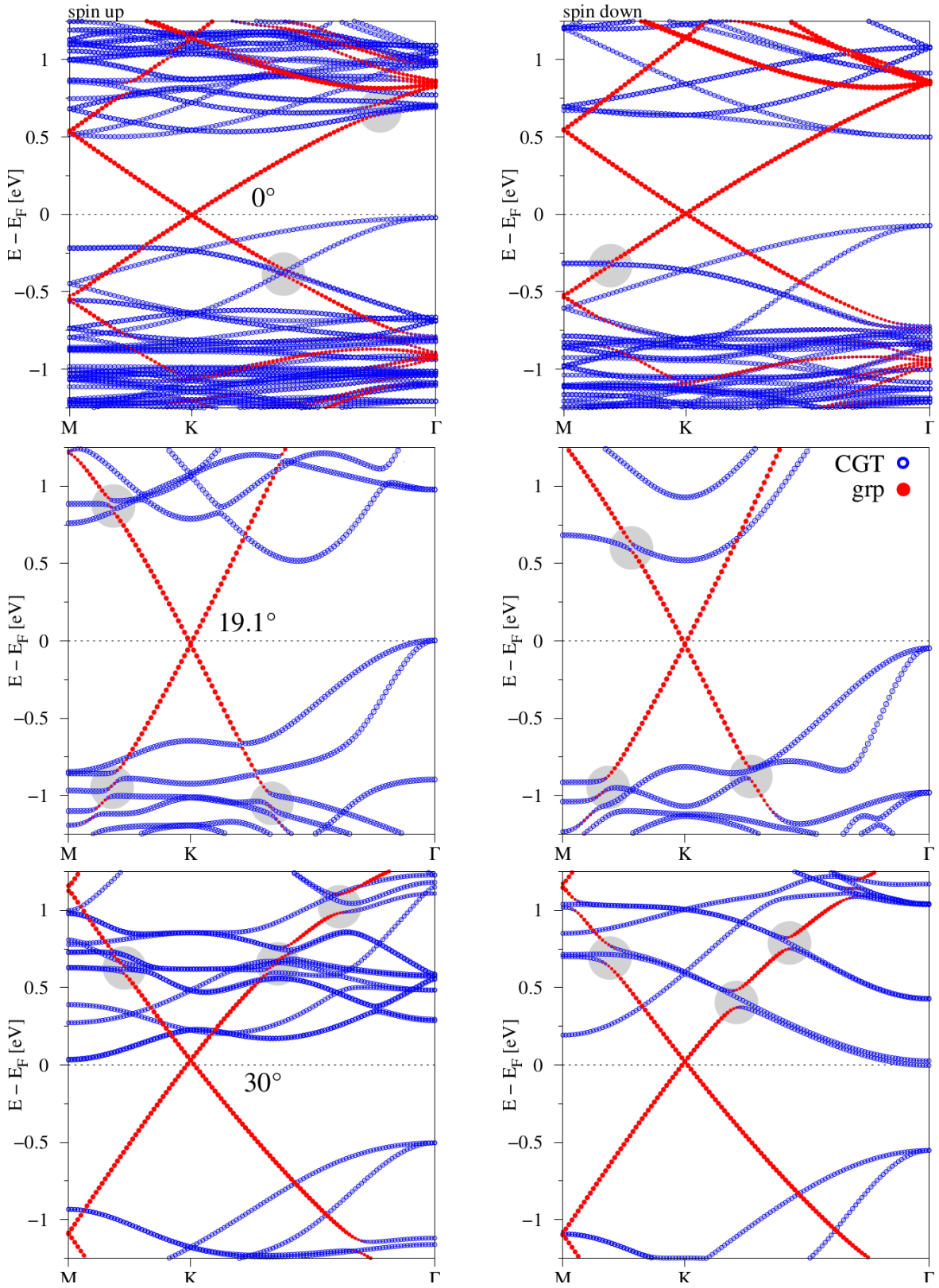

FIG. S18. DFT-calculated projected band structures of the graphene/CGT heterostructures for twist angles of 0°, 19.1°, and 30°. Left: Spin up bands. Right: Spin down bands. We project onto graphene (red) and CGT (blue) states. The grey circles are a guide for the eye to identify band anticrossings, corresponding to interlayer hybridization.

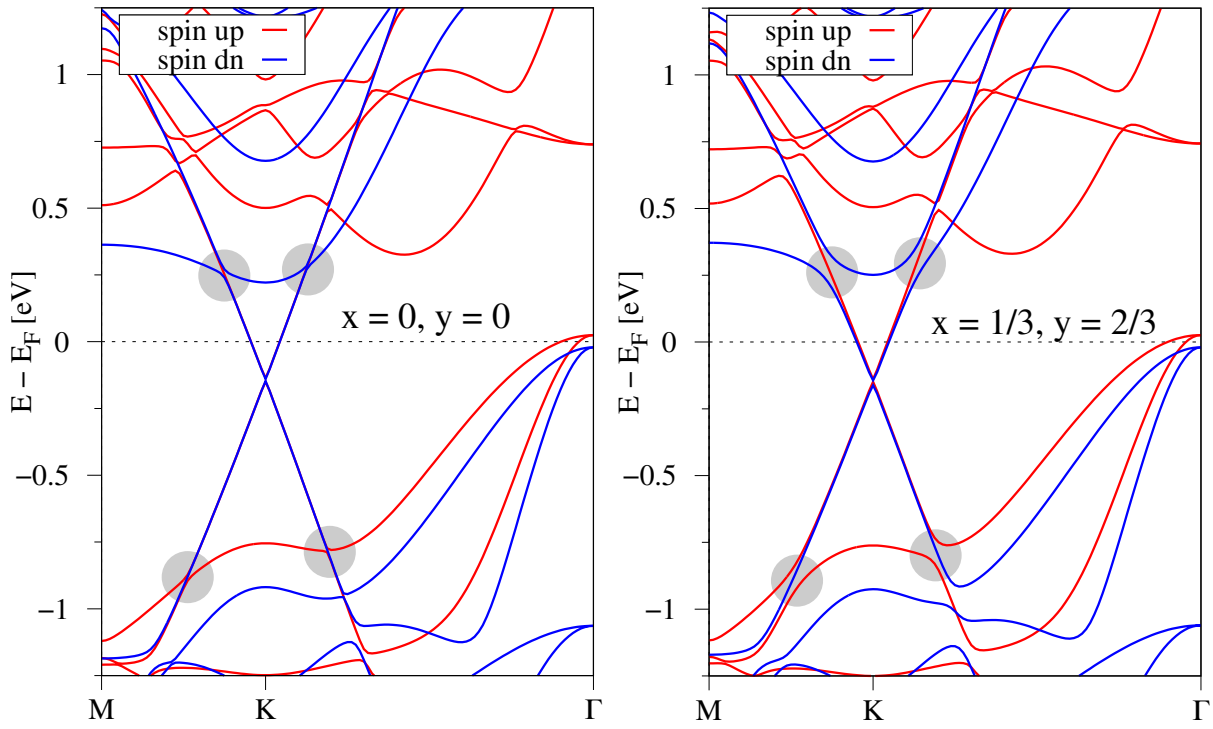

FIG. S19. DFT-calculated band structures of the graphene/CGT heterostructure for a twist angle of 19.1°, but different atomic registries as listed in Table S6. Left: No lateral shift leading to antiferromagnetic proximity exchange. Right: Lateral shift of $x = 1/3$ and $y = 2/3$ leading to ferromagnetic proximity exchange. The grey circles identify four anticrossings, that strongly depend on the atomic registry, and therefore different proximity exchange couplings are realized.

[1] S. R. Bahn and K. W. Jacobsen, "An object-oriented scripting interface to a legacy electronic structure code," Comput. Sci. Eng. **4**, 56 (2002).

[2] Predrag Lazic, "Cellmatch: Combining two unit cells into a common supercell with minimal strain," Computer Physics Communications **197**, 324 – 334 (2015).

[3] Daniel S Koda, Friedhelm Bechstedt, Marcelo Marques, and Lara K Teles, "Coincidence lattices of 2d crystals: heterostructure predictions and applications," The Journal of Physical Chemistry C **120**, 10895–10908 (2016).

[4] Stephen Carr, Shiang Fang, and Efthimios Kaxiras, "Electronic-structure methods for twisted moiré layers," Nature Reviews Materials **5**, 748–763 (2020).

[5] Y. Baskin and L. Meyer, "Lattice constants of graphite at low temperatures," Phys. Rev. **100**, 544 (1955).

[6] V Carteaux, D Brunet, G Ouvrard, and G Andre, "Crystallographic, magnetic and electronic structures of a new layered ferromagnetic compound Cr2Ge2Te6," J. Phys.: Condens. Mat. **7**, 69 (1995).

[7] P. Hohenberg and W. Kohn, "Inhomogeneous electron gas," Phys. Rev. **136**, B864 (1964).

[8] Paolo Giannozzi and et al., "Quantum espresso: a modular and open-source software project for quantum simulations of materials," J. Phys.: Cond. Mat. **21**, 395502 (2009).

[9] Cheng Gong, Lin Li, Zhenglu Li, Huiwen Ji, Alex Stern, Yang Xia, Ting Cao, Wei Bao, Chenzhe Wang, Yuan Wang, Z. Q. Qiu, R. J. Cava, Steven G. Louie, Jing Xia, and Xiang Zhang, "Discovery of intrinsic ferromagnetism in two-dimensional van der Waals crystals," Nature **546**, 265 (2017).

[10] G. Kresse and D. Joubert, "From ultrasoft pseudopotentials to the projector augmented-wave method," Phys. Rev. B **59**, 1758 (1999).

[11] John P. Perdew, Kieron Burke, and Matthias Ernzerhof, "Generalized gradient approximation made simple," Phys. Rev. Lett. **77**, 3865 (1996).

[12] Jiayong Zhang, Bao Zhao, Yugui Yao, and Zhongqin Yang, "Robust quantum anomalous hall effect in graphene-based van der waals heterostructures," Phys. Rev. B **92**, 165418 (2015).

[13] Klaus Zollner, Marko D. Petrović, Kapildeb Dolui, Petr Plecháč, Branislav K. Nikolić, and Jaroslav Fabian, "Scattering-induced and highly tunable by gate damping-like spin-orbit torque in graphene doubly proximitized by two-dimensional magnet $cr_2ge_2te_6$ and monolayer ws_2," Phys. Rev. Research **2**, 043057 (2020).

[14] Bogdan Karpiak, Aron W. Cummings, Klaus Zollner, Marc Vila, Dmitrii Khokhriakov, Anamul Md Hoque, André Dankert, Peter Svedlindh, Jaroslav Fabian, Stephan Roche, and Saroj P. Dash, "Magnetic proximity in a van der Waals heterostructure of magnetic insulator and graphene," 2D Mater. **7**, 015026 (2019).

[15] Stefan Grimme, "Semiempirical gga-type density functional constructed with a long-range dispersion correction," J. Comput. Chem. **27**, 1787 (2006).

[16] Stefan Grimme, Jens Antony, Stephan Ehrlich, and Helge Krieg, "A consistent and accurate ab initio parametrization of density functional dispersion correction (DFT-D) for the 94 elements H-Pu," J. Chem. Phys. **132**, 154104 (2010).

[17] Vincenzo Barone, Maurizio Casarin, Daniel Forrer, Michele Pavone, Mauro Sambi, and Andrea Vittadini, "Role and effective treatment of dispersive forces in materials: Polyethylene and graphite crystals as test cases," J. Comput. Chem. **30**, 934 (2009).

[18] Lennart Bengtsson, "Dipole correction for surface supercell calculations," Phys. Rev. B **59**, 12301 (1999).

[19] Xingxing Li and Jinlong Yang, "CrXTe 3 (X = Si, Ge) nanosheets: two dimensional intrinsic ferromagnetic semiconductors," J. Mater. Chem. C **2**, 7071 (2014).

[20] Xiaofang Chen, Jingshan Qi, and Daning Shi, "Strain-engineering of magnetic coupling in two-dimensional magnetic semiconductor crsite3: Competition of direct exchange interaction and superexchange interaction," Phys. Letters A **379**, 60 (2015).

[21] Johannes Christian Leutenantsmeyer, Alexey A Kaverzin, Magdalena Wojtaszek, and Bart J van Wees, "Proximity induced room temperature ferromagnetism in graphene probed with spin currents," 2D Mater. **4**, 014001 (2016).

[22] Petra Högl, Tobias Frank, Klaus Zollner, Denis Kochan, Martin Gmitra, and Jaroslav Fabian, "Quantum anomalous hall effects in graphene from proximity-induced uniform and staggered spin-orbit and exchange coupling," Phys. Rev. Lett. **124**, 136403 (2020).

[23] Talieh S. Ghiasi, Alexey A. Kaverzin, Avalon H. Dismukes, Dennis K. de Wal, Xavier Roy, and Bart J. van Wees, "Electrical and thermal generation of spin currents by magnetic bilayer graphene," Nature Nanotechnology (2021), 10.1038/s41565-021-00887-3.

[24] Balint Fülöp, Albin Marffy, Simon Zihlmann, Martin Gmitra, Endre Tovari, Balint Szentpeteri, Mate Kedves, Kenji Watanabe, Takashi Taniguchi, Jaroslav Fabian, Christian Schönenberger, Peter Makk, and Szabolcs Csonka, "Boosting proximity spin orbit coupling in graphene/wse_2 heterostructures via hydrostatic pressure," arXiv:2103.13325 (2021).

[25] Balint Fülöp, Albin Marffy, Endre Tovari, Mate Kedves, Simon Zihlmann, David Indolese, Zoltan Kovacs-Krausz, Kenji Watanabe, Takashi Taniguchi, Christian Schönenberger, Istvan Kezsmarki, Peter Makk, and Szabolcs Csonka, "Transport measurements on van der waals heterostructures under pressure," arXiv:2103.14617 (2021).

[26] Tribhuwan Pandey, Avinash P. Nayak, Jin Liu, Samuel T. Moran, Joon-Seok Kim, Lain-Jong Li, Jung-Fu Lin, Deji Akinwande, and Abhishek K. Singh, "Pressure-induced charge transfer doping of monolayer graphene/mos2 heterostructure," Small **12**, 4063–4069 (2016).

[27] Klaus Zollner and Jaroslav Fabian, "Bilayer graphene encapsulated within monolayers of ws_2 or $cr_2ge_2te_6$: Tunable proximity spin-orbit or exchange coupling," arXiv:2103.15378 (2021).

[28] Yang Li and Mikito Koshino, "Twist-angle dependence of the proximity spin-orbit coupling in graphene on transition-metal dichalcogenides," Phys. Rev. B **99**, 075438 (2019).
[29] Alessandro David, Péter Rakyta, Andor Kormányos, and Guido Burkard, "Induced spin-orbit coupling in twisted graphene–transition metal dichalcogenide heterobilayers: Twistronics meets spintronics," Phys. Rev. B **100**, 085412 (2019).
[30] Klaus Zollner, Martin Gmitra, Tobias Frank, and Jaroslav Fabian, "Theory of proximity-induced exchange coupling in graphene on hbn/(co, ni)," Phys. Rev. B **94**, 155441 (2016).